

Preparation of Small Atomic Ensembles in a Fiber Cavity

Lukas Ahlheit

Masterarbeit in Physik
angefertigt im Institut für Angewandte Physik

vorgelegt der
Mathematisch-Naturwissenschaftlichen Fakultät
der
Rheinischen Friedrich-Wilhelms-Universität
Bonn

Oktober 2020

I hereby declare that this thesis was formulated by myself and that no sources or tools other than those cited were used.

Bonn,
Date

.....
Signature

- 1. Gutachter: Prof. Dr. Dieter Meschede
- 2. Gutachter: Prof. Dr. Simon Stellmer

Contents

1	Introduction	1
2	Atom Counting with Fluorescence Imaging	3
2.1	The Experimental Apparatus	3
2.1.1	Cavity-assisted Atom Transport	4
2.1.2	Spread of Atoms in the Conveyor Belt	5
2.2	Raman Cooling Imaging Inside a Fiber Resonator	6
2.3	Image Analysis	8
2.3.1	Sub-pixel Determination of Atom Positions	9
2.3.2	Determination of Local Atom Fluorescence	12
2.4	Towards Resolving the Atom Number in Small Ensembles	14
3	Drive-Through Loading of Multiple Atoms	17
3.1	Compression of Atomic Clouds in Optical Dipole Traps	17
3.2	Numerical Simulation of a One-dimensional Atom Transport	19
3.3	Loading Probability of Drive-through Transport	22
3.4	Simulation-based Optimization of Drive-through Loading	25
4	Loading Small Atomic Ensembles into the Cavity	29
4.1	Measurements of Drive-through Loading	29
4.1.1	Experimental Implementation	29
4.1.2	Optimization of Atom Loading Probability	31
4.2	Benchmarking of Three Loading Techniques	32
5	Discussion and Outlook	35
	Bibliography	37
A	Assembly of a High-NA Imaging System	41
B	Monitoring Vacuum Pressure and Cavity Finesse	49

Introduction

The field of quantum theory started early in the 20th century and grew into an important field in modern physics. The invention of the laser [1] not only allowed to perform experiments to verify fundamental physics, but also triggered the field of *quantum technology*. The term quantum technology encapsulates applications ranging from performing quantum algorithms with the bulk nuclear magnetic resonance technique [2, 3], quantum computing with ions [4], quantum cryptography [5–7] to novel ideas like a large scale quantum network [8–10].

The exchange of information, e.g. qubits, is a key feature of quantum networks. The communication between stationary network nodes can be facilitated by transferring photons via optical fibers as they interact weakly with the environment and are transmitted at the speed of light. However, long distances are challenging to bridge in larger networks, because loss channels can diminish the information fidelity. Regular amplification of the signal is not possible due to the no-cloning theorem for quantum states [11]. Therefore, a scheme for teleportation of quantum states was introduced [12], involving *quantum repeaters* [13] at the network nodes. A quantum repeater requires information transfer from a photonic state to so called platforms such as atoms [14], ions [15], vapors [16, 17] or crystals [18].

Neutral atoms localized into a 3D lattice are an ideal quantum repeater platform, because of their high degree of control [19]. The light-matter interaction between the flying photonic qubit and the confined atom can be enhanced by placing the atom inside an optical cavity. The interaction between an atom and the cavity can be quantified by the coupling rate g . The so called high coupling regime can be achieved by a small cavity mode volume ($g \propto 1/\sqrt{V}$), which is the feature offered by Fiber-based Fabry-Pérot Cavities [20]. As a big step towards quantum repeaters, photon storage experiments have been performed with single atoms coupled to a high-finesse cavity [21, 22]. The storage efficiency can be improved by coupling multiple atoms to the cavity as the interaction rate scales as $g \propto \sqrt{N}$ [23], where N is the number of atoms coupled to the cavity. The techniques for controlling and manipulating neutral atoms in optical lattices have been studied extensively and allow for loading atoms in the center of the cavity mode [24–28]. For multi-atom experiments, it is a prerequisite that different atoms have similar coupling strength to the cavity.

In our experiment, single Rb^{87} atoms are loaded from a background vapor into a magneto-optical trap (MOT). An overlapping optical lattice is used to transport the atoms from the MOT into the cavity, by using the conveyor belt technique [29]. Inside the cavity, the atoms are confined vertically by a blue-detuned intra-cavity lattice and the horizontal confinement is achieved by two red-detuned orthogonal lattices. In place, the atoms are cooled by the technique of degenerate Raman side band

cooling [30, 31] followed by carrier-free Raman resolved sideband cooling [32]. The strong coupling of single atoms to the resonator [33] and storage of short light pulses [34] has been achieved in the past.

In this work, I report on the imaging and preparation of small atomic ensembles inside our fiber cavity. In Chapter 2, non-destructive techniques for determining the number of atoms loaded into the mode of the cavity are presented. Fluorescence images obtained via Raman cooling imaging [35] are analyzed by means of atom position determination and fluorescence integration. Furthermore, a non invasive and resource efficient multi-atom loading technique, based on atom accumulation at the orthogonal lattice crossing under continuous transport, is proposed. The method is studied by a classical 1D numerical simulation in Chapter 3, to explore the parameter space and dynamics of this loading technique. In Chapter 4, the implementation of the novel loading technique is explained and measurement results are compared to the numerical findings. Finally, it is compared to two alternative loading methods and their spatial loading distributions are analyzed.

Atom Counting with Fluorescence Imaging

The method of fluorescence imaging in our setup is elaborated in order to count atoms inside the cavity. First, the experimental setup and optical system is explained. At the same time, a single atom cavity-based detection scheme is introduced. Afterwards, our imaging technique is described. Detailed insight into the system is gained by the analysis of obtained fluorescence images towards the goal of determining the number of atoms coupled to the cavity.

2.1 The Experimental Apparatus

Our experiment is based on coupling ^{87}Rb atoms to a fiber resonator. A top view of the setup is depicted in Figure 2.1a). The cavity is oriented perpendicular to the xy -plane and located at the crossing point of two red-detuned dipole traps. The atoms are confined inside the cavity mode by a three-dimensional lattice. In the horizontal plane, the confinement is given by two orthogonal dipole traps, operating at $\lambda_{x,y} = 868 \text{ nm}$, denoted as $\text{DT}_{x,y}$ respectively. The horizontal beams are focused by a set of four high-NA lenses. The lens-cavity system is introduced in Ref. [36]. In the course of an internship before the thesis work, I aligned a set of four lenses and the alignment procedure is described in Appendix A. The lattice beams along the y -axis are focused into the cavity, whereas DT_x is focused at an offset of $-275 \mu\text{m}$ with respect to the cavity center. One in-vacuum lens is used for collecting fluorescence on the rubidium D1 line, which is sent onto an electron multiplying charge-coupled device¹ (EMCCD) camera. The imaging on the D1 line of rubidium was implemented to be off-resonant with the cavity, which is resonant to the D2 line [37]. The view onto the setup along the imaging axis is shown in Figure 2.1b). Through one of the high-NA lenses the lattice along the x -axis is visible. Along the cavity axis, a standing wave DT_z with a periodicity $\lambda_z = 770 \text{ nm}/2$ defines the atom positions. The same laser is used to stabilize the resonator length by means of the Pound-Drever Hall technique [38].

A typical sequence starts with atom loading from a background vapor at pressure $7 \times 10^{-11} \text{ mbar}$ into a magneto-optical trap (MOT) [39, 40]. Over time, the pressure in the vacuum chamber increases and limits the lifetime of atoms trapped in the dipole trap due to collisions with the background gas. The change of pressure over the course of this work is shown in Appendix B. In addition, the reduction

¹ iXon EMCCD camera: *Ixon 3 DU-897-BV* (Andor Technology Ltd).

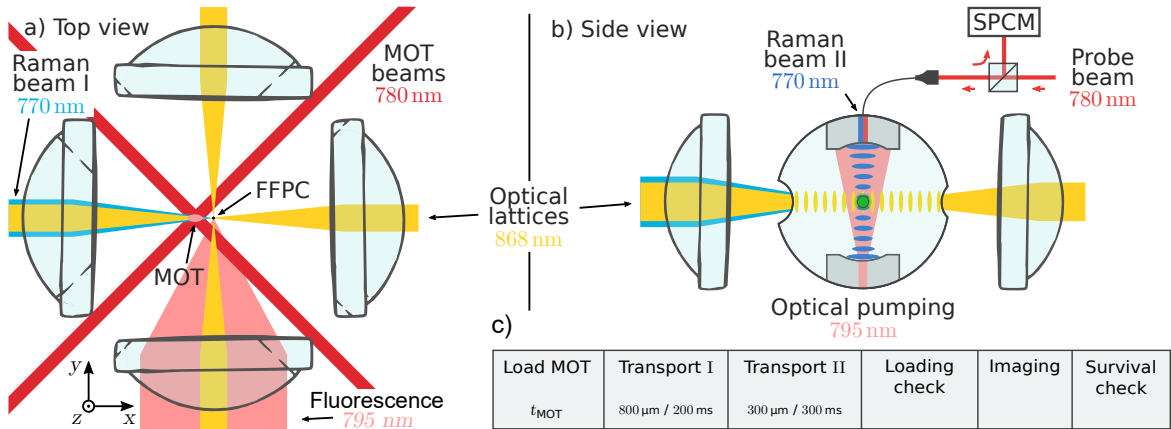


Figure 2.1: a) Top view of the in-vacuum setup. The Fiber-based Fabry-Pérot cavity (FFPC) is placed in the focal point of a set of four high NA lenses. The atoms are horizontally confined in a 2D-lattice created by four dipole trap beams (yellow). A sequence starts with loading atoms into a MOT, about 1 mm away from the cavity, and subsequent transport using the conveyor belt along the x -axis. Raman beam I (blue) send in from the left is used for Raman cooling imaging and the fluorescence is collected by one of the lenses. b) Side view of the in-vacuum setup. One of the horizontal lattices and the intra-cavity lattice (blue) is depicted. Through the top fiber, the Raman laser II and the probe laser are coupled into the cavity. The single photon counter module (SPCM) detects reflected probe photons. Raman beam II and the off-resonantly in-coupled optical pumping laser are used for imaging. For a more detailed introduction see main text and Ref. [41]. c) Loading sequence for the feedback transport.

of the resonator finesse alongside the pressure is shown. A degrading and dissolving glue, which is used to combine the lenses and the cavity to a rigid system, could be a reason. The degradation of the finesse can be slowed down by UV illumination and recovered partially by filling the vacuum chamber with oxygen, see Appendix A.2 in Ref. [36].

The MOT is ~ 1 mm displaced from the cavity center, as it is sketched in Figure 2.1a). One of the lattices is overlapped with the MOT and acts as a conveyor belt [26, 29] in order to transport atoms into the fiber resonator. The atom number loaded into the lattice sites of the conveyor belt is controlled by the loading time of the MOT. The axial spread of atoms follows a Gaussian probability distribution. The overlap with the dipole trap results in a string of a few atoms in the transport trap. By controlling the relative phase of the two counter-propagating beams we are able to displace the atom distribution along the x -axis. This provides means to move the atoms from the MOT location into the fiber cavity with a transport velocity v_{tr} . As the MOT lies out of range of our imaging system, the loading can only be analyzed after transport into the cavity region. The cavity enables the possibility, next to fluorescence images, to detect the presence of an atom in the imaging region.

2.1.1 Cavity-assisted Atom Transport

A typical atom loading sequence is depicted in Figure 2.1c). The MOT loading duration t_{MOT} determines the number of atoms loaded into the dipole trap. Transport I spans 800 μm in 200 ms and transfers the atoms approximately 200 μm before the cavity. Subsequently, the transport is continued with a velocity of 1 mm/s. This transport can be stopped conditioned onto an atom coupling to the

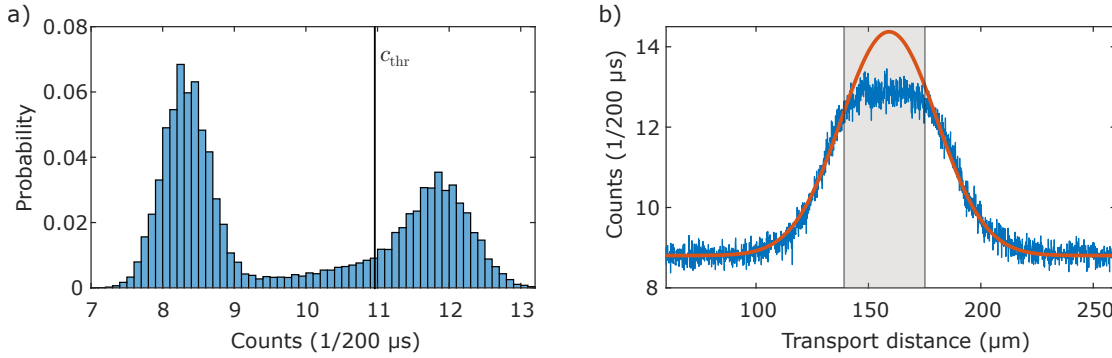


Figure 2.2: a) Count histograms on the single photon counter module for no (left distr.) or at least one (right distr.) coupled atom after a finished transport sequence. The distribution for present atoms has a tail originating from atoms being lost during probing as well as different coupling strength depending on the atom positioning with respect to the cavity mode. The threshold c_{thr} ensure a separation between background and signal cases of a measurement. b) Magneto-optical trap size estimation. The mean reflected counts as function of transported distance is shown. The shape arises from the Gaussian probability distribution with which the atoms are loaded from the magneto-optical trap into the overlapped dipole trap.

cavity [42] and is therefor denoted as feedback transport.

Continuously during the transport, the *probe laser* (780 nm) is send into the top fiber and its reflection from the upper cavity mirror is monitored on a *single photon counter module* (SPCM), see Figure 2.1b). For no atom present in the cavity, the resonant probe photons can enter the cavity. This yields a low number of detected photons on the SPCM. If the transport brings an atom into the cavity, the two couple and as a result the respective eigenenergies split, known as *vacuum Rabi splitting*. The resonance properties of the cavity change and probe photons are reflected from the upper cavity mirror. Accordingly, the level of detected photons increases and the presence of an atom is identified. The atom transport in the conveyor belt is stopped conditioned on a high count level on the SPCM (see [36]). A histogram of counts on the SPCM integrated to 5 ms bins is shown in Figure 2.2a). During transport II, the amount of detected photons in these bins is monitored. The transport stops, if the counts exceed a threshold level c_{thr} .

A second atom coupling to the cavity increases the vacuum Rabi splitting, but not reflection signal on the SPCM. This is saturated by one coupled atom and, hence, the number of atoms can not be determined by this technique. The number determination will be performed by analyzing fluorescence images and is described in the next section. Nevertheless, the reflection signal is used for studying loading and survival probabilities with single atoms.

2.1.2 Spread of Atoms in the Conveyor Belt

The spread of atoms in the lattice is given by the size of the MOT which is transferred into the lattice trap. The width of the MOT distribution on-axis of the conveyor belt can be extracted by analyzing the cavity reflection signal during transport. For these measurements, the transport is not stopped by the cavity reflection feedback. A mean trace of detected photons within 200 μs is shown in Fig 2.2b). Time converted into transported distances yields the full width at half maximum (FWHM) of the MOT distribution as $d_{\text{fit}} = (71.0 \pm 0.7) \mu\text{m}$ from the depicted Gaussian fit. Data within the gray shaded area

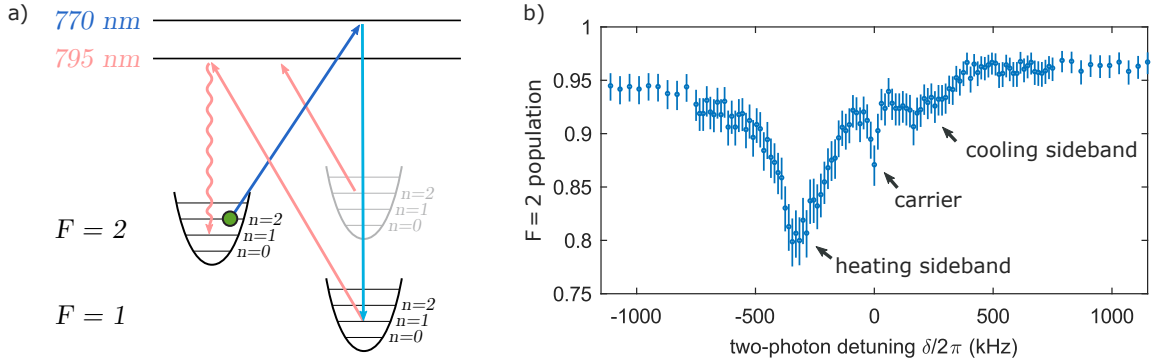


Figure 2.3: a) Raman cooling imaging scheme with one depicted cooling cycle. An atom starts in the upper hyperfine ground state ($F = 2$) with $n = 2$ motional quanta. The depicted Raman transition (blue arrows) is tuned into resonance with the cooling sideband in order to remove one motional quantum as the atom is transferred to the lower hyperfine state. An optical pumping beam on the D1 transition (795 nm) serves as repumper. The emitted photon in the spontaneously decay to $F = 2$ is used to obtain fluorescence images as the cooling continues. b) Raman spectrum after Raman cooling imaging yields a vanishing cooling sideband and indicates near ground state cooling.

is excluded as the saturation is a technical effect, meaning multiple atoms, sitting in neighboring lattice sites, result in several single atom high count features overlap in time. The outcome overestimates the size, as a spatial drift of the MOT acts as an effective broadening. The distance difference of the first and last high bin per trace yields a more precise result. For a threshold of 11 counts per bin, the width is determined as $d_{\text{diff}} = (61.8 \pm 0.9) \mu\text{m}$. This result matches the previously estimated size, see Ref. [36].

Once loaded into the cavity, the atoms are cooled by degenerate Raman sideband cooling [31]. Subsequently, the number of atoms are determined by fluorescence images. The imaging technique has to yield a sufficient *signal-to-noise ratio* (SNR) to distinguish atom numbers.

2.2 Raman Cooling Imaging Inside a Fiber Resonator

In our experiment, fluorescence images are obtained from the Raman cooling imaging technique as it is implemented in Ref. [35]. The technique was already implemented [43] and optimized [44] in our setup. A short introduction is presented here. The level configuration and required optical beams are depicted in Figure 2.3a). From obtained fluorescence images, the optical setup is characterized and theoretical as well as experimental resolution limits are discussed.

Atoms loaded into the cavity are prepared in the hyperfine state $|F = 2, m_F = -2\rangle$ by optical pumping. Due to its non-zero temperature, the atom has n motional quanta distributed in the three dimensions. The motional state can be reduced via properly tuned Raman transitions. The lambda transition transfers the atom into $|F = 1, m_F = -1\rangle$ and depending on the two photon detuning δ its motional state is changed accordingly. The Raman transition is driven by the intra-cavity lattice DT_z and an additional Raman beam I. The transition with $\Delta n = -1$ ($\Delta n = 0, \Delta n = +1$) is denoted as cooling (carrier, heating) transition. In order to repeat the process until the atom is cooled into

the motional ground state ($n = 0$), the atom is optically repumped into the $F = 2$ manifold. The optical pumping beam is resonant to the D1 line of rubidium ($\lambda_{\text{OP}} = 795 \text{ nm}$) and excites the atom to $|F' = 2\rangle$. Subsequently, the atom can decay into $|F = 2, m_F = -2\rangle$, conserving the motional state. The unwanted decay into a different hyperfine level ($m_F \neq -2$) is compensated by the *polarizer beam*. Emitted photons from the spontaneous decay are collected by the high-NA lens and produce an image on the camera. The small fluorescence rate and collection efficiency ($\sim 2\%$) require exposure times of up to 1 s.

The introduced schemes reduces the motion of the atoms in all three dimensions, if the three cooling sideband frequencies are matched. Therefore, Raman spectroscopy was used to calibrate the trap frequencies of the optical dipole traps along the three spatial directions and overlap the cooling transition at 350 kHz [43]. The Raman spectrum in Figure 2.3b) shows that the depth of the cooling sideband is significantly reduced compared to the depth of the heating sideband. The analysis presented in this thesis works with the optimized Raman cooling imaging as elaborated in Ref. [44].

From the recorded images, insight into our imaging system is gained. The magnification is characterized by using the possibility to transport atoms in between two consecutive images. A well defined transport distance d_{magn} can be related to the shift of atom positions s_{magn} in terms of camera pixel. As one pixel has dimensions of $16 \times 16 \mu\text{m}^2$, the magnification is calculated as

$$M_{\text{tr}} = \frac{s_{\text{magn}}}{d_{\text{magn}}} \cdot \frac{16 \mu\text{m}}{1 \text{ pixel}}.$$

Here, M_{tr} denotes the magnification is obtained by intermediate transport. A transport of $2 \mu\text{m}$ was applied in between the two background subtracted images shown in Figure 2.4a). The atom location shift is retrieved by calculating the cross-correlation of the two images for both axis separately. Therefore, the cross correlation is calculated for the projections onto the respective axis [37]. Both mean cross-correlation of many two image sets is shown in Figure 2.4b). From the position of the maxima, the total pixel shift is calculated by $s_{\text{magn}} = \sqrt{s_x^2 + s_z^2}$. The magnification of our optical system is $M_x^{\text{tr}} = 34.9$. Therefore, $0.46 \mu\text{m}$ correspond to one camera pixel.

The resolution limit is given by the *point spread function* (PSF), which describes how a perfect point source is imaged in an optical system. The Rayleigh criterion determines the minimum resolvable detail in an optical system limited by diffraction. From there, the spatial resolution can be quantified in terms of the Abbe-radius, defined as $d_{\text{Abbe}} = 0.61 \frac{\lambda}{NA}$. Here, NA denotes the numerical aperture, a characterization for the system capability of focusing light. In our setup, we have lenses with $NA = 0.5$ and the imaging is performed with 795 nm photons. The theoretical resolution limit is $d_{\text{Abbe}} = 970 \text{ nm}$. In the experiment, the resolution reduces due to an effectively smaller NA and optical aberrations. In order to infer information about the resolution in the experiment, single atom images are used to reconstruct the PSF. Therefore, a mean single atom image is shown in Figure 2.4c). A 2D fitted Gauss gives the standard deviation in terms of camera pixel, which can be converted with the magnification to $\sigma_{\text{PSF}} = 0.785 \pm 0.002 \mu\text{m}$.

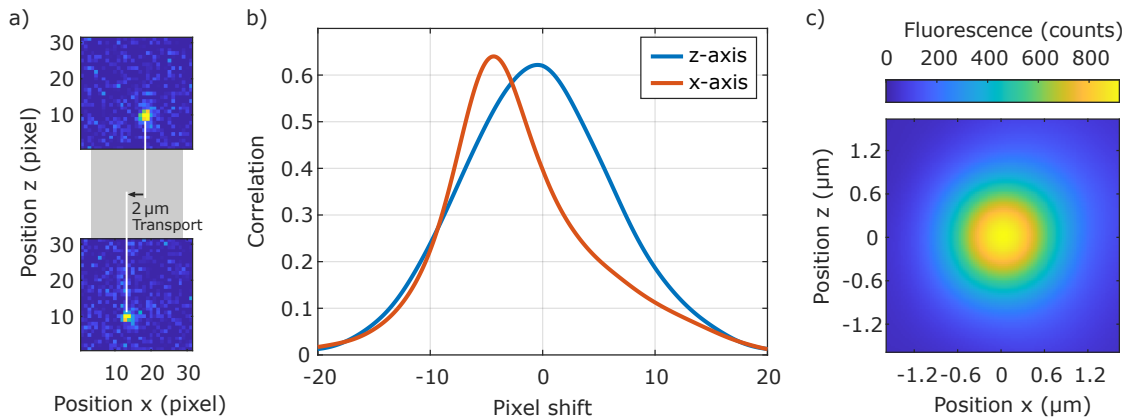


Figure 2.4: a) Two background subtracted images recorded before and after an intermediate transport. b) Mean cross correlation between the projection onto the x - and z -axis of both images per sequence respectively. The position of the maximum in terms of pixel shift can be related to the transported distance to find the magnification of our optical system. c) Point spread function of our imaging system.

2.3 Image Analysis

The integrated fluorescence per image is used to determine the number of atoms loaded to the cavity. Noise, arising from stray light and scattered light from the upper cavity mirror (see Ref. [44]), is broadly distributed over the images, which hampers the number determination of atoms. This effect can be overcome, if the position of atoms in the image is known. Integrating the fluorescence locally around a detected atom greatly reduces the background influence.

In this section, it is presented how images are processed to determine the atom position. Furthermore, a method for extracting atom locations with sub-pixel resolution is presented. With regard to counting atoms, the technique for integrating the fluorescence locally around detected peaks is introduced.

Images are obtained from the EMCCD camera in terms of incident fluorescence photon counts integrated over time per pixel. Internally the incident photons are converted into electrons with a quantum efficiency of 75%. The electron registers can be amplified, set by the *electron multiplying* (EM) gain.

The first step in the image analysis is subtraction of a mean background, which is extracted from experiment runs without an atom present in the cavity. For that, the capability for detecting the atom presence with the cavity, independent from fluorescence images, is utilized. The cavity based atom detection is used to determine signal and background images. For a signal image, an atom is required to be present before and after the imaging duration. An image needs on the other hand the absence of an atom in both check in order to be labeled as background image. The subtraction removes counts from static light sources. The main contribution of background arises from deflected optical pumping photons. The amount depends on the incident optical pumping beam power. A typical background subtracted image is shown in Figure 2.5a).

The atoms oscillate within the lattice and can hop between lattice sites. Both effects result in atoms spread over several pixel, even if about 1 lattice site per pixel is expected according to the calculated magnification. Therefore, the brightest pixel does not necessarily coincide with the center of mass

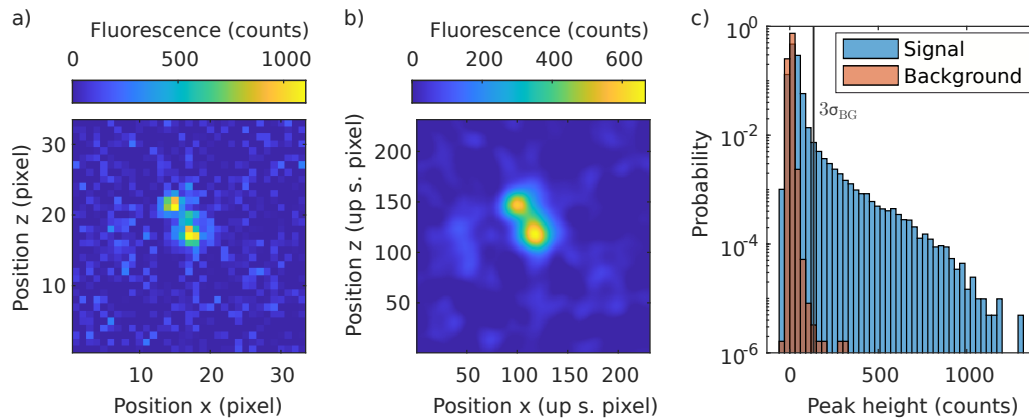


Figure 2.5: a) Example of a background subtracted image. b) The same image as a) after upsampling by a factor 7 and Gaussian filtering ($\sigma_{\text{filter}} = 1$ pixel). c) Probability histogram of heights for detected peaks in the upscaled signal and background images.

position of the atoms. The peak localization is improved by smoothening the image with a Gaussian filter. The filter width σ_{filt} is chosen as one pixel and the filter size is set to $5 \times 5 \text{ pixel}^2$, which samples a Gaussian distribution very coarse. In order to improve the smoothening, the image is upscaled by a factor $S \times S$. Meaning, each original pixel is replaced by S pixel of the same height and, subsequently, the rescaled image is smoothed by the filter. The standard deviation and kernel size are scaled respectively. The resolution enhancement can be retraced in Figure 2.5b). In the upscaled images, regional maxima can be determined by `imregionalmax` in MATLAB, which returns a binary image of peak locations. A peak is defined as pixel with all surrounding ones being lower in amplitude. In the processed images, peaks arising from atoms (atom peaks) as well as peaks in the background are detected. The two can be separated, because typically atom peaks inherent higher count numbers on the camera. Atom peaks are selected by a count threshold c_{thr} , which is calculated from the spread of peak heights in background images. The distribution of detected peaks in background images is shown in Figure 2.5c) in red. The width of the background distribution is obtained from a Gaussian fit and determines the threshold to $c_{\text{thr}} = 3\sigma_{\text{BG}}$. The factor of 3 separates the background and signal peaks well such that less than 0.1 % of all detected peaks can be attributed to the background. The monotonous decrease of peak height probabilities in signal images above the threshold points towards detecting different amount of fluorescence for different atoms. Similar detected fluorescence from all atoms should create a peak in the signal histogram at the respective total single atom fluorescence.

The depicted PSF in Figure 2.4c) is obtained by overlapping 62 single atom images. The images are upscaled by a factor of 17 and the obtained peak locations are used to overlay the images.

2.3.1 Sub-pixel Determination of Atom Positions

In this section, the method for determining the position of atoms with sub-pixel resolution in the fluorescence images is introduced. Furthermore, the lattice is reconstructed, giving rise to a second measure of the magnification as well as the orientation of lattices with respect to the camera.

² The MATLAB function `imgaussfilt` chooses the kernel size suited for a given Gaussian standard deviation.

The accuracy of atom position determination in the upscaled image is in discrete steps. In order to find the atom positions with sub-pixel resolution, a sum of n_p 2D Gaussians (see Eq. 2.1) is fitted to images with n_p detected peaks exceeding the threshold.

$$I_{2D, Gauss}(x, z) = \sum_{i=1}^{n_p} A_i e^{-((x-x_i)^2+(z-z_i)^2)/\sigma_i^2} \quad (2.1)$$

Here, the amplitude A_i and the standard deviation σ_i are free parameters, in addition to the atom coordinates. A symmetric Gaussian with a single standard deviation σ_i per peak is chosen, because a symmetric approach is a valid approximation to the PSF (see Figure 2.4c)).

The lattice gives rise to a periodic spatial distribution $f(z)$ of the atoms, which can be described as [45]

$$f(z) = \frac{1}{N} \sum_{i=1}^N \delta(z - z_{\text{det},i}), \quad (2.2)$$

where, $z_{\text{det},i}$ is one of all possible N atom position in the images. The periodicity of $f(z)$ can be deduced from its Fourier transform

$$\text{FT}\{f(z)\} = \frac{1}{\sqrt{2\pi N}} \sum_{i=1}^N e^{2\pi i k z_{\text{det},i}} \quad (2.3)$$

as it peaks at integer multiple of the spatial frequency k_0 .

For a set of 10159 images, the positions along the cavity (z_i) and transport axis (x_i) are obtained from fitting Gaussians. Only images with less than 6 peaks ($n_p \leq 5$) are considered, which makes up 99.8 % of all images. The chance of peaks overlapping is high for many peaks per image and, therefore, the number of reasonable fits is reduced. The following analysis focuses on the z -axis, as experimental limitations for the transport axis hinder the method. For this measurement, the feedback transport was used, which implies that the lattice stops in arbitrary positions with respect to the imaging region. This effect as well as phase jitters of the lattice result in unreproducible atom positions. The position histogram along the cavity axis is shown in Figure 2.6a). The intra-cavity lattice has a periodicity of 385 nm and from the magnification a peak bunching every 1.19 pixel is expected. In the outer parts of the histogram, the atom position clustering is visible. The site positions are only distinguishable in the outer pixel, because there the depth distribution of atoms with respect to the focal plane is restricted by the available lattice sites within the focal depth. In the central pixel, the atoms can be placed further away from the focal plane resulting in blurring of peaks. Therefore, the localization of atoms to the standing wave wells can not be retraced in the histogram.

The introduction of Gaussian fits opens the possibility to consider only well coupled and imaged atoms, as the confidence interval of the fitting parameters indicate the quality of the fit. Therefore, fits with the confidence intervals for x_i , z_i and σ_i exceeding a certain boundary can be neglected. This increases especially the visibility of the regular structure in the central part (see red histogram in Figure 2.6a)). Nevertheless, it is not as evident as in the outer image part. A reason can be that the lattice along the imaging axis, created by DT_z , has an angle with respect to the imaging path, which would wash out peak positions projected onto the focal plane. Furthermore, the conditioning of fits is

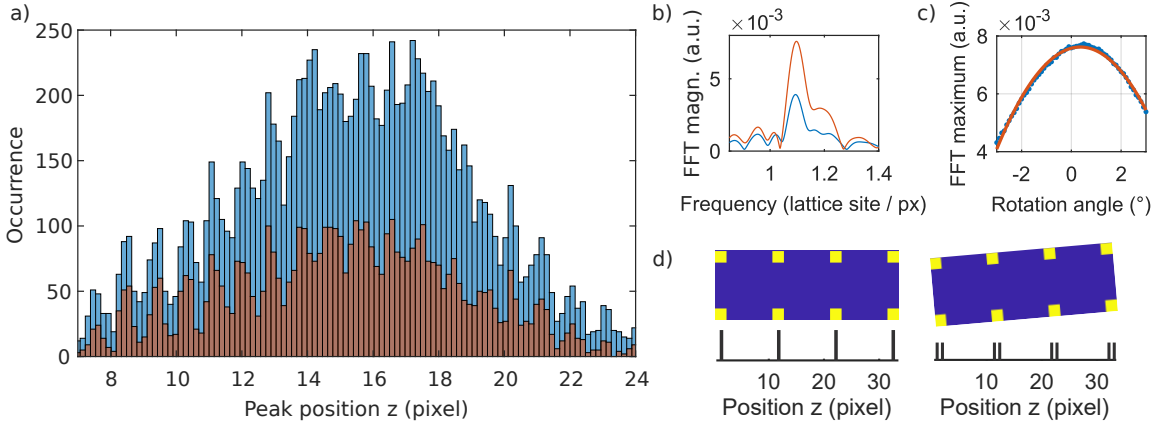


Figure 2.6: a) Position histogram of detected peaks (blue) along the cavity axis, obtained from fitting a sum of Gaussians to each processed image. A lattice structure is more prominent, if limits for the confidence intervals of fitting parameters are applied (red histogram). b) Fourier transform of the histograms in a). The conditioning of fits increases the Fourier amplitude. Note, the frequency implies more than one lattice site per original image pixel. c) Height of the Fourier transform in b) for a prior coordinate system rotation. For a perfect alignment between the cavity lattice and the camera pixels the histogram peaks in a) are sharp and wash out for any angle, see schematic in d).

not foolproof and lattice drifts over time hamper the lattice reconstruction additionally.

In order to obtain the periodicity, the two histograms are transformed to Fourier space and the signal is depicted in Figure 2.6b). The parameter confidence interval conditioning of the fits enhances the frequency component. The frequency represents how many lattice sites correspond to a single pixel and can yield information on the magnification of the system along the z -axis.

$$M_{\text{FT}} = \frac{1 \text{ pixel}}{1.097 \text{ lattice site}} \cdot \frac{16 \mu\text{m}}{1 \text{ pixel}} \cdot \frac{1 \text{ lattice site}}{385 \text{ nm}} = 37.9$$

Here, the frequency of 1.097 trapping sites per pixel is extracted from the Fourier signal. The known size of a lattice site along the cavity axis and the dimension of a camera pixel result in a slightly different magnification as obtained from the transport of atoms.

The sub-pixel determination of atom positions can also be used to study the orientation of our optical lattices with respect to the camera pixel arrays. The lattices can have an angle with respect to the camera, which washes out the atom position projected onto one of the camera axes, see schematic in Figure 2.6d). The 2D coordinate system can be rotated by θ

$$\begin{pmatrix} x' \\ z' \end{pmatrix} = \begin{pmatrix} \cos(\theta) & \sin(\theta) \\ -\sin(\theta) & \cos(\theta) \end{pmatrix} \begin{pmatrix} x \\ z \end{pmatrix} \quad (2.4)$$

and the retrieved histogram exhibits the sharpest features, if θ matches the angle between lattice and camera axis. The height of the Fourier transform for different rotation angles is depicted in Figure 2.6c). An angle of $\theta_z = 0.36^\circ$ between the cavity lattice and the camera is obtained from fitting a second order polynomial. Further information on reconstructing 2D lattices and extracting their orientation from fluorescence images can be found in literature [45, 46].

In order to extract lattice structures from fluorescence images, the lattices have to be stable. The lattice along the cavity axis is invariable over long times, as the same signal is used to stabilize the length of the cavity. This translates into a stabilized and constant standing wave pattern along the z -axis. On the other hand, the DT_x is used to transport the atoms into the cavity and the feedback transport of atoms results in varying lattice phases on two consecutive images. This could be overcome by extending the analysis method to extract distances of detected peaks in a single image (see e.g. [45, 46]). For our experiment, the obtained distance histograms are not exhibiting any clustering of atoms at multiple of the lattice periodicity. A reason could be the cumulative uncertainty of two fits hindering the distance determination. For the distance analysis, it is required to have two or more atoms per image. The statistics are reduced, because all involved fits have to fulfill the parameter confidence interval bounds.

The introduced technique for peak position determination can not be used to count atoms inside the cavity, especially for an increased number of atoms, as the depth information is missing. This implies two atoms sitting behind each other along the imaging axis are counted as a single atom. The fluorescence around the single detected peak should be twice the single atom fluorescence and open the possibility to count atoms. Therefore, the position determination is combined with integrating the fluorescence around detected peaks in the following part.

2.3.2 Determination of Local Atom Fluorescence

The number of atoms placed in the cavity can be inferred from the detected total fluorescence on the camera. The region of interest (ROI) for the imaging is chosen as 33×33 pixel, because this covers the waist diameter of the cavity and the radial center of the transport trap. The histogram of integrated fluorescence in this *static region of interest* (sROI) is depicted in Figure 2.7b). The blue histogram is obtained from signal images. In contrast, background images require atom absence in both cavity-based checks. From all images a mean background is subtracted and, therefore, the background histogram is centered around zero. The large spread of the background histogram indicates that noise is present in all images. The overlap of the histograms limits the fidelity of fluorescence based determination to no or one present atom.

In order to enable atom number determination, the fluorescence integration is combined with the peak localization described in the previous section. The fluorescence is not integrated in the full static ROI, but in an *adaptive region of interest* (aROI) generated from the knowledge of detected peak positions. An example image with three detected peaks is shown in Figure 2.7a). Here, 5×5 patches are depicted around each peak. The separate masks are unified to create an image mask within which the fluorescence is integrated. The histogram of integrated fluorescence in the aROI is shown in Figure 2.7c), for the same data as b). Moreover, the background is also masked with the same sized patches. Since there are no distinct peaks in the background, the patches are located iterative at all pixels with subsequent fluorescence integration. The spread of the background histogram in the smaller regions is much less, enabling a separation of events with zero and at least one atom based on the emitted fluorescence.

Only single images with one detected peak are considered in the following analysis. The separation of signal and background histogram for the two integration methods (sROI & aROI) can be quantified in two ways. First off, the overlap between the histograms is extracted. For the static ROI, the overlap is

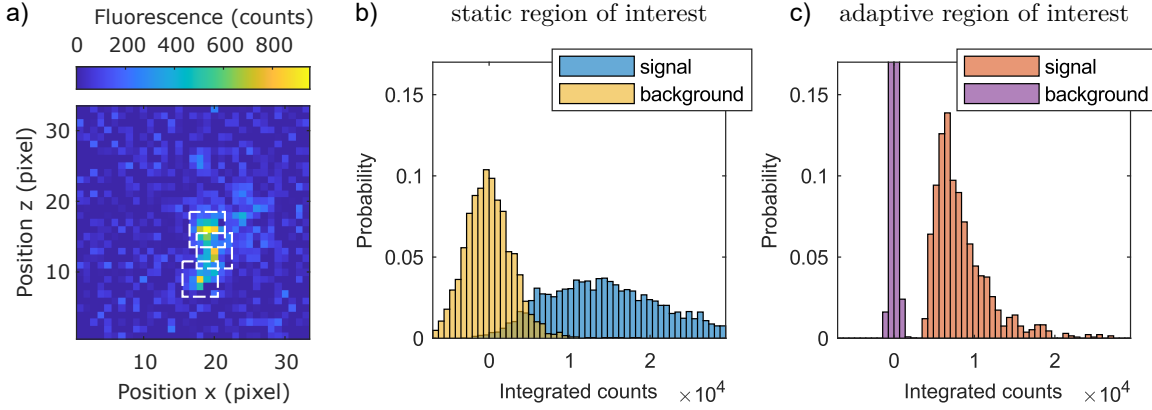


Figure 2.7: a) Fluorescence image of three atoms. The white rectangles are placed around detected peak positions and are used to create an adaptive region of interest (aROI) for integrating fluorescence counts. b) Histogram of integrated fluorescence in a static ROI (sROI, 33×33) for signal and background images. From all images a mean background is subtracted. Atom counting from the signal histogram is not possible, as the signal histogram should inherent peaks at integer multiple of the single atom fluorescence. The broad background and its overlap with the signal motivate a more versatile technique to avoid integration over a lot of background. c) Same data set as b), but the fluorescence is integrated in an adaptive ROI (5×5) around detected peaks. Separation of no atom possible, nevertheless no atom counting realizable.

around 11.8 %. The adaptive ROI greatly improves it to 0.001 % for a mask size of 5×5 pixel. The overlap is studied for different mask sizes in Figure 2.8a), see orange graph. The dashed horizontal line indicates the overlap obtained from the static ROI integration. On the other hand, the so called *signal-to-noise ratio* (SNR) is a measure for the separation of two histograms and is given by

$$\text{SNR} = \frac{\mu_{\text{Signal}}}{\sigma_{\text{BG}}},$$

where, μ_{Signal} is the mean integrated background-subtracted signal and σ_{BG} the spread of the background. The naive approach with the static ROI yields $\text{SNR} = 5.28$. The signal to noise ratio for the adaptive ROI is $\text{SNR} = 12.78$ and its scaling with the mask size is depicted in Figure 2.8a). For mask sizes larger than 5×5 pixel, the SNR saturates as most of the emission from an atom is considered and the background spread is increasing linearly with the size. From these two figures of merit the optimum mask size is chosen as 5×5 pixel².

The presented analysis for the best mask size used a count threshold of $3 \sigma_{\text{BG}}$ as already introduced. The threshold applies a truncation on the left side of the signal histogram and, therefore, has an influence on the overlap of signal and background histogram. For different thresholds, the number of peaks per image and the overlap between the histogram of mean peak fluorescence in signal images and the background histogram is calculated and depicted in Figure 2.8b). At low thresholds many peaks arising from noise are detected in signal images and, thereby, the number of detected peaks per image increases strongly below a threshold of 100 counts. All potential peaks not arising from atoms yield a low integrated fluorescence and this results in the observed larger overlap with the background histogram. The criterion of $3 \sigma_{\text{BG}}$ is strong enough to not consider many background peaks.

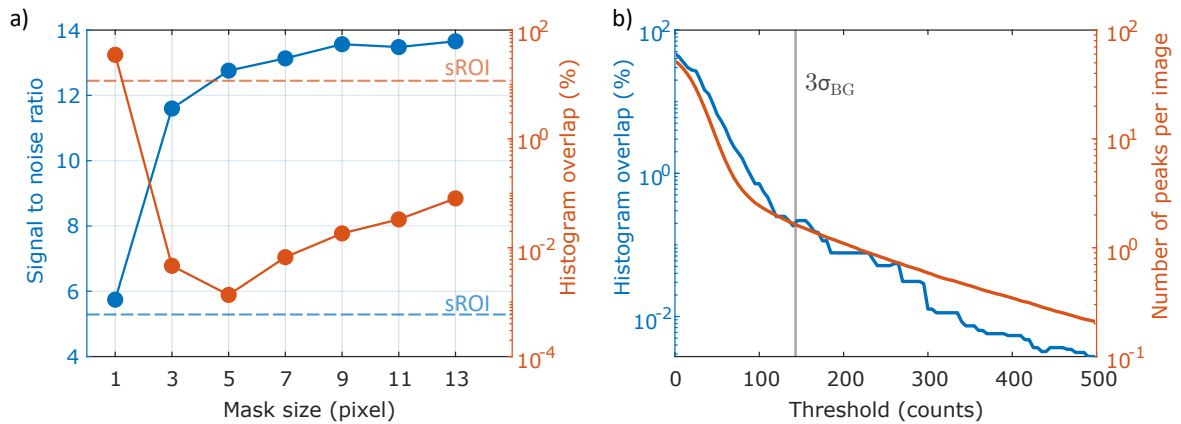


Figure 2.8: a) Mask size analysis for histogram of integrated fluorescence within adaptive ROI. In blue, the signal-to-noise ratio saturates for mask sizes above 5 and surpasses well the one obtained from the static ROI (dashed line). Furthermore, the overlap of signal and background histogram (orange) is minimized for a mask size of 5×5 pixel. In b), the threshold is changed for a fixed mask size of 5. The signal histogram is different from a) as it considers the mean fluorescence per peak in an image. The overlap greatly increases below three times the spread of the background. At the same time, the number of detected peaks per image is rising.

From the presented fluorescence histograms, the number of atoms in the imaging region can not be determined reliably. Despite the fact that the influence of the noisy background was minimized. The spatial resolution gained by the images can be used in order to investigate the spatial dependence of the single atom fluorescence further.

2.4 Towards Resolving the Atom Number in Small Ensembles

The presented image analysis provides detailed insights into the experimental setup. It is used to investigate which effects hamper the atom number determination.

Separation of the Mean Image

The mean of all fluorescence images, shown in Figure 2.9a), yields little information, because it is a product of three different quantities:

$$\text{mean image} = \text{position distribution} \times \text{fluorescence distribution} \times \text{survival probability distribution}.$$

Here, the *position distribution* gives the probability for an atom to be loaded at a certain position. For this analysis, the peak locations are plotted in a 2D histogram, depicted in Figure 2.9b). The threshold for peak detection is set rather low in order to avoid missing out dim peaks. This analysis reveals that the atoms are mostly loaded into an small area around pixel ($x = 23$, $z = 18$). This position is the crossing point of the conveyor belt, along the x -axis, and the cavity mode, along the z -axis. The atoms are transport from left to right and the cavity-based feedback stops the first atom inside of the resonator and, hence, the rest of atoms loaded from the MOT distribution into the conveyor belt is

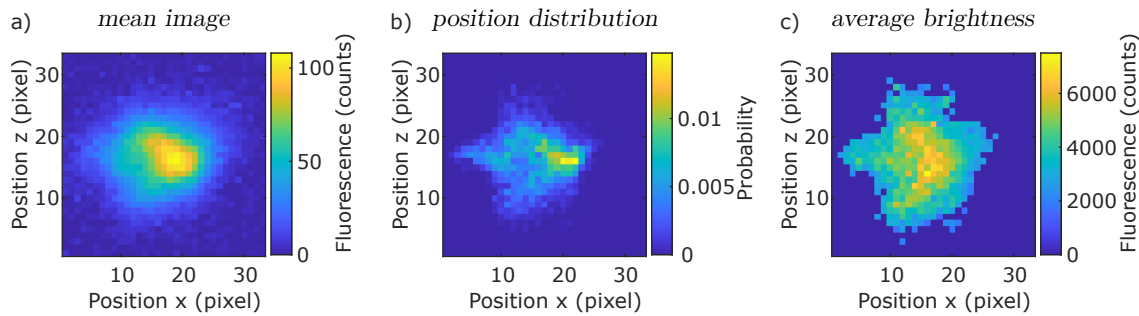


Figure 2.9: Separation of a) the mean image into b) the position distribution and c) average brightness given by the fluorescence distribution and the survival probability. The cavity mode is centered about $x = 23$ pixel.

distributed on the left. In addition, this results in very low loading probability for positions $x > 25$ pixel.

Second, the average *fluorescence distribution* of an atom located in a certain camera pixel can be extracted. The fluorescence around isolated peaks is obtained and the mean fluorescence of atoms being located in a certain pixel is retrieved. In order to avoid overlapping patches of too closely detected peaks only single atom images are considered. The fluorescence distribution in Figure 2.9c) differs significantly from the position distribution. Over the imaging region, the atom fluorescence varies by a factor of 2 and yields a maximum fluorescence of about 7000 counts within the one second integration.

Finally, the *survival probability distribution* of atoms has to be taken into account. An atom lost from the trapping potentials and moving out of the imaging region would result in a detected peak with lower total fluorescence. Therefore, Figure 2.9c) shows the product of average fluorescence and survival probability.

Narrowing the Inhomogeneous Distribution of Fluorescence

A control over the position spread of atoms within the average fluorescence map would be an important step towards atom number determination in ensembles inside the cavity. It is of special interest for future experiments to have similar coupling of all atoms to the cavity. We found a method for spatial selection of atoms in the radial direction of the cavity mode. The atoms can be heated depending on their radial position in the mode. The trapping frequency of the atoms reduces radially away from the mode center. By modulating the intra-cavity lattice at twice the trapping frequency, the atoms can be parametrically heated out of the lattice. The tuning of the modulation frequency allows the removal of atoms above certain radii around the cavity mode center and only the well coupled ones remain.

Drive-Through Loading of Multiple Atoms

In this chapter, a loading technique for small atomic ensembles into the fiber resonator is introduced. To form these ensembles inside the cavity, the density of atoms has to be increased by applying a compression technique within the loading sequence. First, established experimental techniques for realizing atomic ensembles and their applicability in our experiment are discussed. Second, a 1D simulation of the conveyor belt transport is introduced that will be used to investigate a new combined loading and compression technique - the *drive-through loading*. The underlying processes and the involved critical parameters relevant for the experimental implementation are identified. In the end of this chapter, the optimal parameters for loading of small atomic ensembles are presented. The experimental realization and comparison to the numerical findings is presented in the last chapter of this work.

3.1 Compression of Atomic Clouds in Optical Dipole Traps

In order to perform experiments with atoms confined in optical lattices, their loading probability in terms of spatial spread and density are of interest, especially if the optical access is limited as in our setup. In the following, a few loading and compression techniques are introduced and the feasibility of using them within our setup with two crossed dipole traps overlapped inside a fiber resonator is analyzed.

Time-dependent Lattice Compression

A simple configuration would be to load the MOT inside of the cavity where experiments will be performed. There, the atom distribution can be compressed by modifying the superimposed dipole trap configuration [47]. Atoms are loaded into a single large scale well of an optical lattice, created by two lattices crossed with a small angle. The site is decreased in size by increasing the angle and the atomic cloud is compressed. Afterwards, the atom distribution could be loaded into a symmetric 2D optical lattice. However, the associated tuning of the dipole trap angles is not possible in our configuration.

Compressed MOT

An alternative method could be based on the principle of a compressed MOT as realized in Ref. [24]. There, the atom distribution inside the MOT is compressed by increasing the field strength of the trapping field. Subsequently, the compressed MOT could be loaded into an optical trap. This technique requires the MOT loading at the location of later experiments, which is inside of the fiber cavity for our setup. The small cavity geometries given by the fiber diameter of $125\ \mu\text{m}$ and resonator length of $\sim 93\ \mu\text{m}$ [36] have to be considered and clipping of the necessary beams for the MOT would be unavoidable. This would heat the fibers and result in unstable resonator properties. Therefore, creating the MOT inside of the cavity is not an option.

Quarter Cycle Compression

A MOT outside of the cavity requires a transport in addition to the desired compression. In our setup, the MOT could be loaded into one of the 1D optical lattices in the horizontal plane. The atoms would be rather broadly distributed along the lattice. Following a technique implemented in Ref. [48], the atoms could be compressed around the focal point of the dipole trap. As described in the reference, atoms roll towards the deepest point of the conservative potential, if one of the lattice beams is switched off. After a quarter of the oscillation period in the running wave, a reestablishment of the lattice gives rise to atoms populating sites close to the trap focal point. It has to be considered that the compressed atom distribution along the lattice should be located inside of the cavity. Therefore, the focal point of the lattice should be inside of the fiber resonator. In our setup, the dipole beam is focused between the cavity and the MOT. This configuration was chosen to have proper potential depth during the transport in order to minimize atom losses. The mismatch of MOT location and optical lattice focal point would require a subsequent transport after the introduced compression.

A general limitation on how many atoms can be compressed in a one dimensional lattice is denoted for high atom number (see Ref. [48]). Loading many atoms increases the probability for two atoms populating the same site after compression, resulting in both atoms being lost from the trap. This could be overcome by introducing a three-dimensional lattice and, hence, make more sites available to avoid double occupied sites.

Aside the introduced conventional techniques, we investigated in a for us experimentally more accessible version that makes use of our 3D lattice configuration.

Drive-through Loading

In our setup, atoms are loaded into the DT_x lattice and the following transport is conditionally stopped to load atoms into the cavity, see Section 2.1.1 on the feedback transport. It was observed that sometimes atoms were found in the cavity even for disabled conditional transport. As cavity region, the spacial overlap of the two orthogonal lattices in the horizontal plane and the cavity mode is denoted. In one measurement, the conditional transport was disabled and a non-zero probability for an atom to be present in the cavity was observed after a completed transport sequence. Further measurements showed that the probability by changing the potential depth of the transport lattice. More precisely the power ratio of the two crossing dipole traps was changed. The effect of atom accumulation under continuous transport is denoted as *drive-through loading* in the rest of this work.

The effect is analyzed by means of a numerical simulation. First, the simulation should yield insights about the underlying mechanism and how it depends on experimental parameters like the relative depths or transport velocity. Second, different initial parameters are chosen to determine their influence onto the accumulation probability in the cavity region, also denoted as region of interest (ROI).

3.2 Numerical Simulation of a One-dimensional Atom Transport

The simulation models the transport of an atom placed in the potential $U(x, t)$, created by the optical dipole traps. A one-dimensional approach was chosen and turned out to provide sufficient understanding of the drive-through loading. The simulation is based numerical integration of the second Newtonian law of motion $F(x, t) = m \cdot a(x, t)$. The obtained differential equation is integrated numerically for a given set of initial parameters. Thereby, a particle is propagated step by step forward in time taking into account the retrieved position and velocity of a previous time step. The approach can be visualized by the first-order Euler method where the new position and velocity are calculated like

$$\begin{aligned} x(t + dt) &= F(x, t)/2m \cdot dt^2 + v(t) \cdot dt + x(t) \\ v(t + dt) &= F(x, t)/m \cdot dt + v(t) \end{aligned}$$

from the previous time step. In the end, the more complicated fifth-order Runge-Kutta method is used to achieve more accuracy for the resulting particle trajectories.

The force can be related to a potential as $F(x, t) = -\nabla U(x, t)$ in order to simulate the movement of a particle inside of the optical lattice potential. In accordance with the classical picture from Lorentz, the potential arises from dipole interactions between an atom and the electromagnetic field of a laser [49]. The classical one is the simplest approach and it can be justified by comparing the relevant energy scales. All trapping potentials have a depth of tens of μK . This is large compared to the recoil energy, $R = 0.15 \mu\text{K}$, gained from interactions with dipole trap photons [50].

The implementation of cooling in the simulation can yield information on whether the cooling in the experiment during the drive-through loading is beneficial to optimize the overall loading probability. The cooling is introduced as a friction force into the equation of motion (see Eq. 3.1).

$$\frac{d^2}{dt^2}x(t) = \frac{F(x, t)}{m} - \alpha \cdot g(x) \cdot v(t) \quad (3.1)$$

Here, the cooling amplitude is defined by α and $g(x)$ parameterizes the spatial dependence of the cooling strength. The spatial dependence is defined by the mode of the cavity, as the intra-cavity lattice beam is one arm of the involved cooling scheme. Therefore, $g(x)$ is a Gaussian with a standard deviation of $5 \mu\text{m}$.

In the simulation, only the two horizontal dipole traps are considered and the intra-cavity lattice is neglected due to its repulsive character. Overall the potential is expressed as the sum of the two orthogonal trapping potentials. U_t for the transport lattice along the axial direction (Eq. 3.2) and

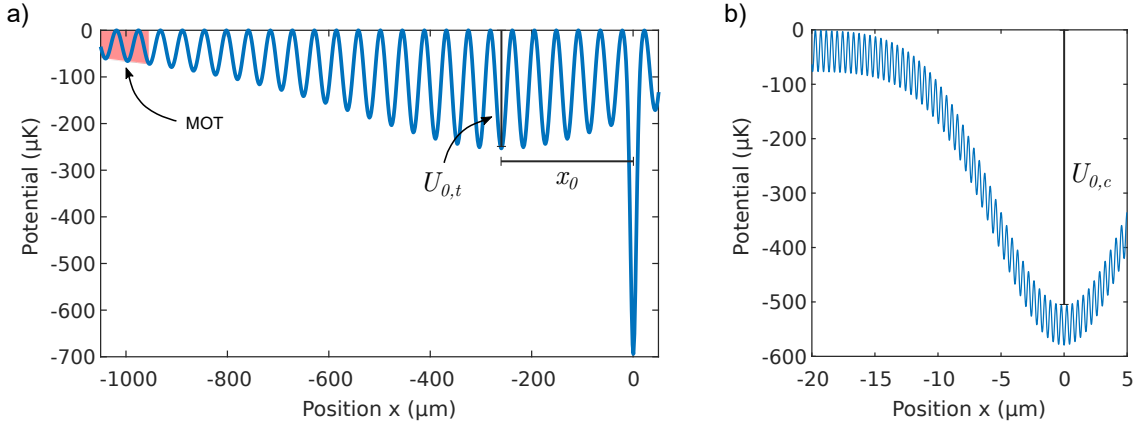


Figure 3.1: One-dimensional representation of trapping potentials. a) Potential along the transport axis created by two crossed dipole traps with a relative depth of $\beta = 0.5$. The lattice wavelength was scaled up by a factor of 100 for visibility of single lattice wells. The transport lattice focal point has an offset of $x_0 = -275 \mu\text{m}$ with respect to the crossing region around $x = 0$. In the experiment, atoms are transported approx. 1 mm from the MOT into the crossed trap. For further details see main text. b) Potential at the crossing region for a relative depth of $\beta = 0.2$. Single lattice sites of the transport trap are visible.

U_c for the crossed trap with a Gaussian transversal shape (Eq. 3.3).

$$U_t(x, t) = U_{0,t} \cdot w_{0,t}^2 / w_{DT}^2(x - x_0) \cdot \cos^2(k_{DT} \cdot (x - x_0) + 2\pi t \cdot v_{tr} / \lambda_{DT}) \quad (3.2)$$

$$U_c(x, t) = U_{0,c} \cdot \exp\left(-2(x/w_{0,c})^2\right) \quad (3.3)$$

Respectively for each trap, U_0 is the lattice depth, k_{DT} is the wave vector and w_0 is the beam waist. The phase factor $t \cdot v_{tr}$ shifts the periodic lattice structure according to a transport velocity v_{tr} . Both traps have a waist radius of around $11 \mu\text{m}$ and a wave length of $\lambda_{DT} = 867 \text{ nm}$. Along the transport axis, the lattice spot size $w_{DT}(x)$ scales as

$$w_{DT}^2(x) = w_0^2 \left[1 + \left(\frac{x}{x_R} \right)^2 \right], \quad x_R = \frac{\pi w_0^2}{\lambda_{DT}},$$

where, x_R is the Rayleigh length. Note, that in Eq. 3.2, a non-zero x_0 changes the transport lattice spot size at the dipole trap crossing $x = 0$ and yields as an effective trap depth scaling. This focal point displacement is fixed in the experiment at $x_0 = -275 \mu\text{m}$ resulting in a spot size $w_{DT}^2(0) = 13 \mu\text{m}$, but is kept as free parameter for the numerical studies. The sum of both potentials is depicted in Figure 3.1a) for a set of parameters close to the experiment. For achieving visibility of single lattice sites, the wavelength of the lattice trap was increased by a factor of 100.

In accordance with Gaussian beam optics, the lattice depths are calculated from beam geometries and powers [25]. One of the most important optimization parameters for the drive-through loading is the relative depth between both traps, defined as $\beta = U_{0,t}/U_{0,c}$. The full depths are $U_{0,t} \approx 0.5 \text{ mK}$ and $U_{0,c} \approx 0.5 \text{ mK}$, respectively, for $\beta = 1$. The crossing region for $\beta = 0.2$ is shown in Figure 3.1b) and the Gaussian macro potential is overlapped with few tens of transport lattice sites. Here, the wavelength of the lattice is not scaled up.

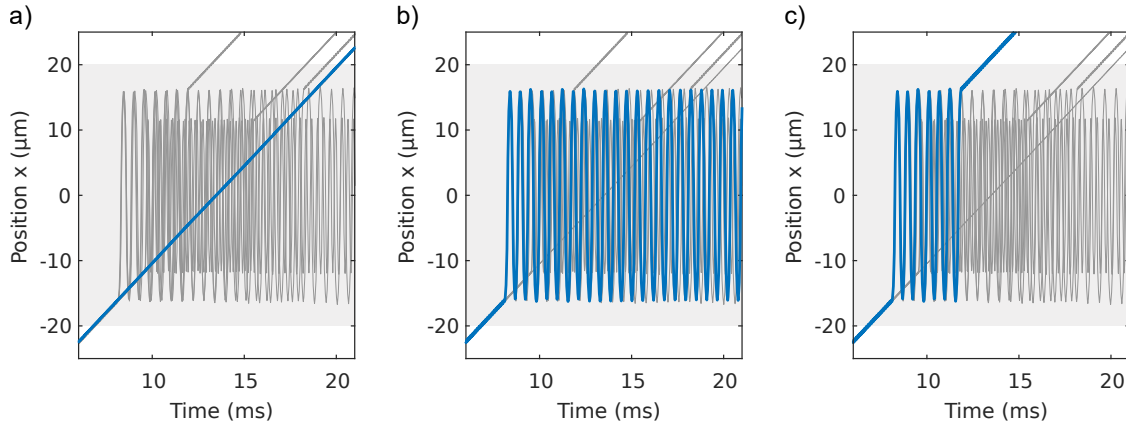


Figure 3.2: From the numerical simulation retrieved particle trajectories. Each simulation starts with a different set of initial position and velocity and in a)-c) three trajectories are highlighted in blue. Particles can perform oscillations around the center of the orthogonal trap $x = 0 \mu\text{m}$ and accumulate in the crossing region ($\pm 20 \mu\text{m}$) indicated in light gray. The fraction of atoms present at the end of the simulation determines the single atom loading probability.

The derivative of the modeled potential is calculated analytically and yields the force to which the atoms are exposed. The MATLAB implementation of this simulation uses a fifth-order Runge-Kutta solver with a fixed time step resolution, following Ref. [51]. Three resulting trajectories, from a larger set of initial position x_i and velocity v_i , are depicted in blue in Figure 3.2a)-c). In light gray the crossing region around $\pm 20 \mu\text{m}$ is indicated. Depending on their initial condition, the particles are either transported linearly through, see trajectory a), or perform oscillations around the center of the orthogonal dipole trap potential, see b) and c). All three trajectories are highlighted from a total set of simulation runs, depicted as the gray trajectories in the background. The single atom loading probability can be deduced from the number of atoms present in the crossing region at the end of the simulation from the total number of trials.

Effective Well Depth Analysis

To gain insight in the underlying process that traps atoms in the orthogonal dipole trap during the drive-through loading, the transport of particle b) in Figure 3.2 is considered in the following. The particle is linearly transported until $x = -20 \mu\text{m}$, where the crossing region is reached and the orthogonal trapping potential has to be considered, see Figure 3.1b). The Gaussian shaped potential from the crossed trap tilts the wells of the lattice potential. In Figure 3.3a), two tilted lattice sites are depicted on the entering slope of the crossed trap. The gray arrows indicate lattice oscillations. If the energy of the particle is higher than the effective well depth U_{eff} , it escapes the site and rolls down the potential hill. After this, the particle starts oscillating around the crossing point at $x = 0 \mu\text{m}$. This means, the particle remains nearby the center and is considered as loaded into the resonator mode. The effective depth sets an energy threshold which particles have to exceed in order to accumulate around the cavity region. This threshold is set by the relative potential depth β and the trap focus displacement x_0 as shown in Figure 3.3b). The dashed lines on top of the contour plot indicate the respective depth U_{eff} in μK . The overlaying colored points in Figure 3.3b) show the drive-through

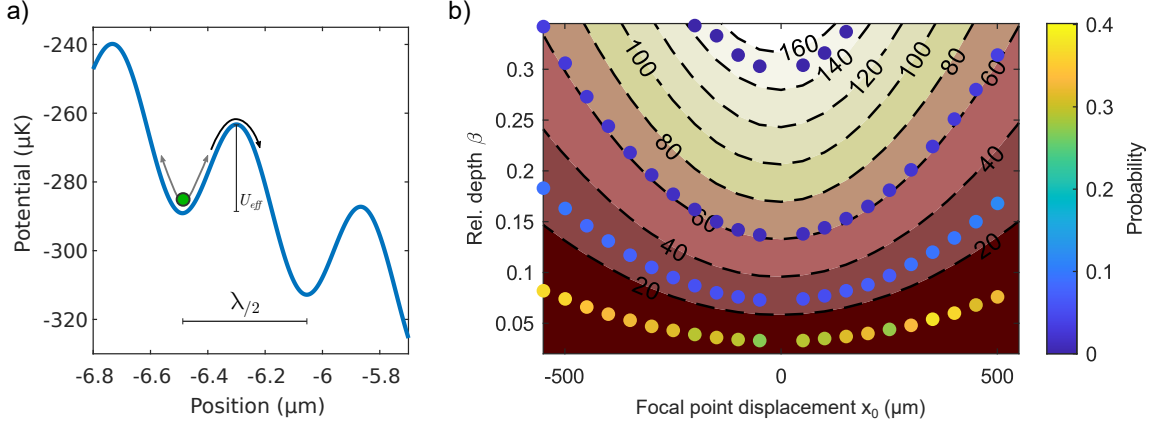


Figure 3.3: Trapping mechanism of the drive through loading technique. a) shows the lattice wells tilted by the potential of the crossed trap. Particles oscillating (gray arrows) with a total energy larger than effective well depth U_{eff} can escape the lattice and start oscillating in the crossed potential. In b) the contour plot shows the effective well depth U_{eff} as function of the relative trap depth β and lattice focal point displacement x_0 . Along one effective depth isoline, the drive-through loading probability is approx. constant as the colored data points indicate. See the main text for details on how the probabilities are obtained from the simulation.

loading probability \mathcal{P}_{DTL} obtained from the simulation. It confirms that the effective depth is the parameter determining, if atoms accumulate in the crossing region. The parameters were chosen such that four so called isolines in terms of the effective depth are sampled. On these lines, the U_{eff} is constant and found from the simulation the loading probability is also constant. The probability higher for lower effective depth, since atoms with smaller initial temperature can be trapped. To investigate the drive-through loading probability \mathcal{P}_{DTL} , the energy barrier U_{eff} will be compared to the mean energy of atoms of a certain temperature within the dipole trap in the following section.

3.3 Loading Probability of Drive-through Transport

The aim for the experiment is to load multiple atoms into the resonator mode. For that, the probability to accumulate in the cavity region for atoms with a given temperature is of interest. This is quantified by the drive-through loading probability \mathcal{P}_{DTL} . This section shows how \mathcal{P}_{DTL} is extracted from the simulations and how the initial distribution of atoms is modeled.

The probability for an atom to leave its well on the slope of the orthogonal trap for a given effective potential is denoted as \mathcal{P}_{DTL} . It is determined by the energy of the atom, if it accumulates around the orthogonal trap or not. Not all atoms loaded from the MOT into the lattice have the same energy. For an atom in a MOT, its probability to have a certain energy is defined by a Maxwell-Boltzmann distribution. In accordance to the one-dimensional model, a 1D Boltzmann distribution is considered. This is a rough approximation from the three-dimensional case as it underestimates the probabilities for high atom energies. The distribution of motional quanta is greatly different in the two consideration. For a certain amount of quanta to distribute, there are more combinations available in 3D, due to the three directions, as in the simpler one-dimensional case. Nevertheless, the 1D Boltzmann is used as

it is the best known approximation at hand. The energy distribution is modeled as the Boltzmann distribution given in Eq. 3.4. Here, the density of states for a harmonic oscillator (HO) is considered in order to approximate the present \cos^2 -lattice. For high energy states, its anharmonicity modifies the density of states compared to a HO. Repeatedly, this approximation underestimates the population of high energy states in the lattice. The systematic error given by both approximations has to be kept in mind for the analysis of the drive-through loading.

$$p(E, \beta) = \frac{1}{k_B T(\beta)} \exp\left(-\frac{E}{k_B T(\beta)}\right) \quad (3.4)$$

Here, k_B is the Boltzmann constant and T the mean atom temperature. The temperature scales with the relative trap depth factor β , whereat this is also known as adiabatic lowering [52]. In short, a lowering of the trap in an adiabatic manner reduces the effective temperature of the atoms like $T_{\text{new}} = \sqrt{\beta}T$. In Figure 3.4a), two Boltzmann distributions are shown for different relative depth. The energy distribution is truncated at energy E_{max} defining the highest possible energy for an atom to be loaded with. Atoms with more energy than the lattice depth are not captured and are therefore not transported. After truncation, the distributions need to be normalized.

The energy maximum arising from the lattice depth at the MOT location is denoted as $E_{\text{max,MOT}}$. The atoms transported towards the crossing region can get lost due to passing shallower lattice wells. The lattice depth can be set by the relative trap depth β and the focal point displacement x_0 , see Figure 3.1a). The shallowest well depth during the transport, before entering the slope of the orthogonal trap, sets a second energy for the distribution truncation. It is denoted as $E_{\text{max,init}}$ in the following. The fraction of atoms loaded at the MOT location and being above $E_{\text{max,init}}$ can be calculated as

$$L = \frac{\int_0^{E_{\text{max,init}}} p(E, \beta) dE}{\int_0^{E_{\text{max,MOT}}} p(E, \beta = 1) dE} \quad (3.5)$$

and specifies the probability for an atom to be lost during the transport. The probability distribution for the shallowest well already considers a lowered lattice. The drive-through loading probability \mathcal{P}_{DTL} is obtained by considering atom loading at the shallowest well. It can be scaled to the total drive-through loading probability $\mathcal{P}_{\text{DTL, total}} = L \cdot \mathcal{P}_{\text{DTL}}$.

In order to model \mathcal{P}_{DTL} , 16 equally spaced energies within $(0.1, 1) \cdot E_{\text{max,init}}$ are considered and the outcome of each is weighted with its probability according to the truncated Boltzmann HO distribution. For one exemplary well, a few levels are depicted in Figure 3.4b). The initial energy can be given by a kinetic and a potential part. The splitting introduces different initial phases for the lattice oscillations. All phases are weighted equally, because there is no favored phase during the loading from the MOT. It is found that the phase has no influence on the probability for an atom to be loaded into the orthogonal trap. Nevertheless, the energy is distributed with 12 phases in order to increase the statistics. The distribution of energy onto potential and kinetic energy is given as

$$\begin{aligned} E_{\text{pot}} &= E_{\text{tot}} \cdot \cos^2(\phi) \\ E_{\text{kin}} &= E_{\text{tot}} \cdot \sin^2(\phi), \end{aligned}$$

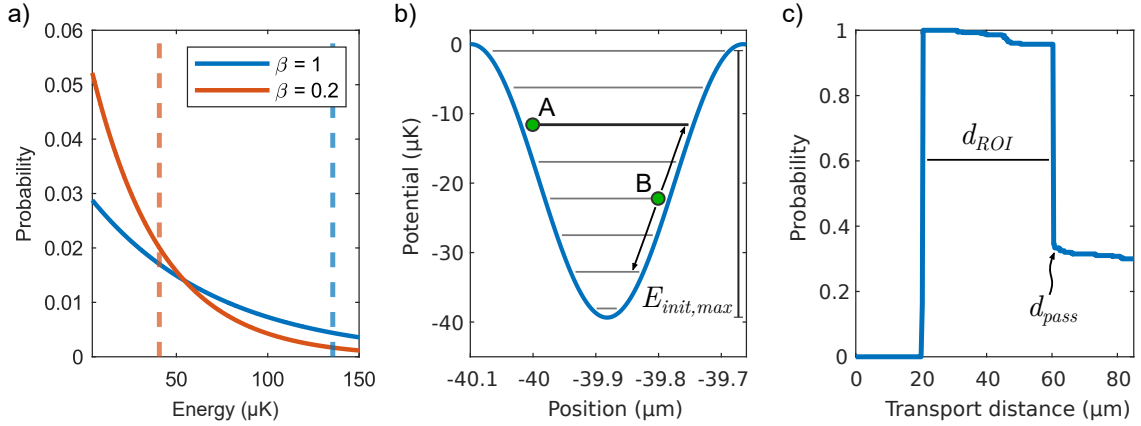


Figure 3.4: a) Two Boltzmann distributions, with $T = 40 \mu\text{K}$, for different relative trap depth β , which effectively modifies the mean temperature. They are truncated at energy $E_{\text{init,max}}$ (dashed lines). b) Initial position and velocity within one lattice site. Particles A and B have the same total initial energy (black level), but its distributed differently into a kinetic and a potential part. The well depth between the starting site and the cavity region defines the maximum initial energy $E_{\text{max,init}}$. Different levels are weighted according to the Boltzmann distribution in a). c) Fraction of particles in the cavity region extracted from the simulation as function of the transported distance. The drive-through loading probability is given by the fraction at $d_{\text{pass}} = 60 \mu\text{m}$, at which all non-accumulating particles are transported through the ROI.

where, ϕ is representing the phase and E_{tot} the total initial particle energy. For the simulation, the potential (kinetic) energy is used to calculate the starting position x_i (velocity v_i). Consider two particles A and B, where A has purely potential energy and starts with zero velocity and B a non-zero velocity, but both particles have the same total energy. Their energy level is marked marked as black horizontal level in Figure 3.4b). The two particles are in a different phase of their lattice oscillation.

Each pair of energy and phase defines the initial parameter for a single simulation run. The separate simulations are combined in order to obtain the loading probability \mathcal{P}_{DTL} . In the post-analysis, a position dependent binary check is performed for each trajectory. A final particle position within $\pm 20 \mu\text{m}$ is denoted as loaded. Each trace is weighted according with the probability for its initial energy. All the traces are overlapped and the time-dependent probability $\mathcal{P}(t)$ for an atom to be in the crossing region can be extract. In Figure 3.4c), the probability is shown as function of the transport distance, as retrieved from the simulation time and the corresponding transport velocity. The drive-through loading probability \mathcal{P}_{DTL} is the fraction of atoms left in the region of interest (ROI) at distance d_{pass} . This distance can be calculated by $d_{\text{pass}} = (|x_i| + d_{\text{ROI}}/2)$, with the size of the ROI $d_{\text{ROI}} = 40 \mu\text{m}$. \mathcal{P}_{DTL} yields as figure of merit to find the optimum loading probability for different experimental parameters.

Validation of the Simulation

In order to show the trustworthiness of the simulation results, different validation tests were performed. In each run of the simulation, the position and velocity of a particle are calculated in time steps of t_{res} . A time resolution of 10 ns is chosen, in order to resolve the fastest position changes. The highest occurring velocity is defined by the involved trap depths. Considering only the crossed trap, with a

depth of 0.5 mK, a particle starting far out converts all the potential energy into kinetic energy while it oscillates through the trap center. There, a maximum velocity of 0.3 m/s is reached. For the given time resolution, a particle at this velocity moves 3 nm, which is small compared to 11 μm , the trap waist radius. The oscillations are well sampled by the simulation and the particle trajectory is correctly calculated.

Next, the simulation was tested on a static potential with $v_{\text{tr}} = 0$ m/s. For that scenario, the total energy of the particle has to be conserved. All deviations from the initial energy E_{init} can be considered to rise from numerical errors. The total energy of the particle is calculated for each time step. After simulating oscillations for different initial conditions for 100 ms, the energy deviates at most by 1 % from the respective initial energy.

Furthermore, it was tested how the solver handles time inversion of the problem. The position and velocity after the evolution for 66 ms serve as the new initial parameters for a simulation with inverted time. The error of final position and velocity compared to the first initial values is 10^{-5} .

The simulation can be transformed into the Galilean frame, in order to test how well the solver handles time dependent forces. The full problem, as described above, is set to a moving frame, in which the particle oscillates in the crossed trap. Its total energy at the end shows a deviation to the initial energy comparable to the static frame result.

All the above described investigations demonstrate that the accuracy of the simulation is fine enough to cover the physical effects we want to investigate.

3.4 Simulation-based Optimization of Drive-through Loading

The simulation is used to estimate the influence of experimental parameters onto \mathcal{P}_{DTL} , in order to optimize the loading in the experiment. Scans of the relative depth β and the transport velocity v_{tr} are presented. Furthermore, the influence of cooling during the transport is discussed.

Relative Trap Depth

As discussed before, the effective well depth strongly influences the drive-through loading probability. In the experiment, the lattice focal point is fixed at $x_0 = -275$ μm and only β is a free parameter. The drive-through loading probability is obtained for a set of relative depths. The result for a transport velocity of $v_{\text{tr}} = 3$ mm/s and a mean atom temperature of $T_{\text{mean}} = 40$ μK is shown in Figure 3.5a). The highest loading probability for an atom is achieved for a relative depth of $\beta = 0.025$. The total probability is calculated from \mathcal{P}_{DTL} using Eq. 3.5 and $\mathcal{P}_{\text{DTL,total}} = L \cdot \mathcal{P}_{\text{DTL}}$. For small β , this strongly decreases the total loading probability, since in a too shallow lattice atoms are not transported and have no possibility to accumulate.

Transport Velocity

The effect of the transport velocity on the drive-through loading probability is investigated. The duration in which the linear transport crosses the cavity region is given by the transport velocity v_{tr} . The simulation for the set of relative depth β discussed before is repeated for different velocities. In

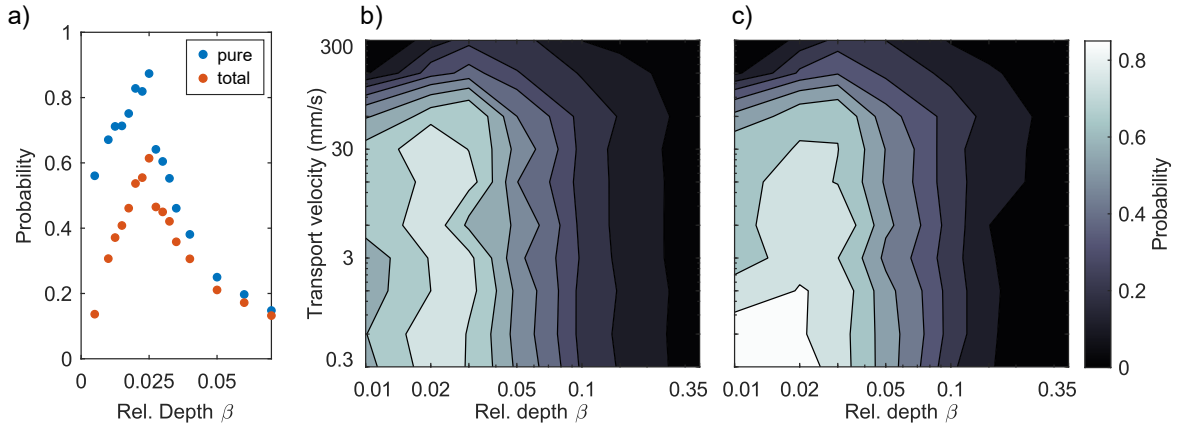


Figure 3.5: a) The drive-through loading probability \mathcal{P}_{DTL} for different relative depth (blue points). In close to 90 % of the cases, an atom is loaded into the resonator. Considering losses during the transport from the MOT reduces the probability for very small β , here denoted as $\mathcal{P}_{\text{DTL, total}}$. b) \mathcal{P}_{DTL} as function of β and the transport velocity. For most v_{tr} , the scaling with the relative depth is consistent with a). At very fast transports, the atoms fly over the crossing region and have no change for accumulation. In c), a cooling in the cavity region, which increased the loading probability for slow transports velocities, was introduced. There, the cooling has enough time to reduce the atom energy. See main text for details on the implementation.

Figure 3.5b), \mathcal{P}_{DTL} is shown for this two parameter scan. The velocity is changed over three orders of magnitude. The probability is mainly insensitive to the velocity of the transport compared to the dependence on the relative depth. Only very fast transports are decreasing the loading probability. v_{tr} is added to the initial particle velocity which can result in a large enough kinetic energy to not be localized within the orthogonal trap.

Cooling Strength

The drive-through loading probability \mathcal{P}_{DTL} as function of the relative depth and cooling strength is shown in Figure 3.6a). Moderate cooling (orange and yellow) increase the loading probability at low relative depth. An atom oscillating upwards on the right slope of the Gaussian shaped potential from the orthogonal trap can get retrapped into a lattice site and transported out. This effect is circumvented by active cooling. The increase in loading probability \mathcal{P}_{DTL} can also be seen in traces of $\mathcal{P}(t)$ for the different cooling strength (see Figure 3.6b)). In the case of strong cooling $\alpha = 1000$ Hz, the drive-through loading probability \mathcal{P}_{DTL} decreases to zero for a slight increase in β . There, the atoms can get localized by the cooling into a lattice well at the center of the orthogonal trap. Within this well, the atoms get transported out and the time-dependent loading trace in Figure 3.6c) (purple) drops very low. Below a certain β , the effective well depth U_{eff} is zero and the atom slips down. This is the reason for the loading probability of unity below $\beta = 0.02$ for the strongest cooling (see purple graph in Figure 3.6a)). From \mathcal{P}_{DTL} , the total drive-through loading probability can be obtained and it is shown in Figure 3.6d) for the same cooling analysis. The tuning of cooling strength does not increase the maximum loading probability, but shifts the peak to lower relative depth.

Figure 3.5c) shows the same two-dimensional scan as in b), but active cooling ($\alpha = 10$ Hz). The

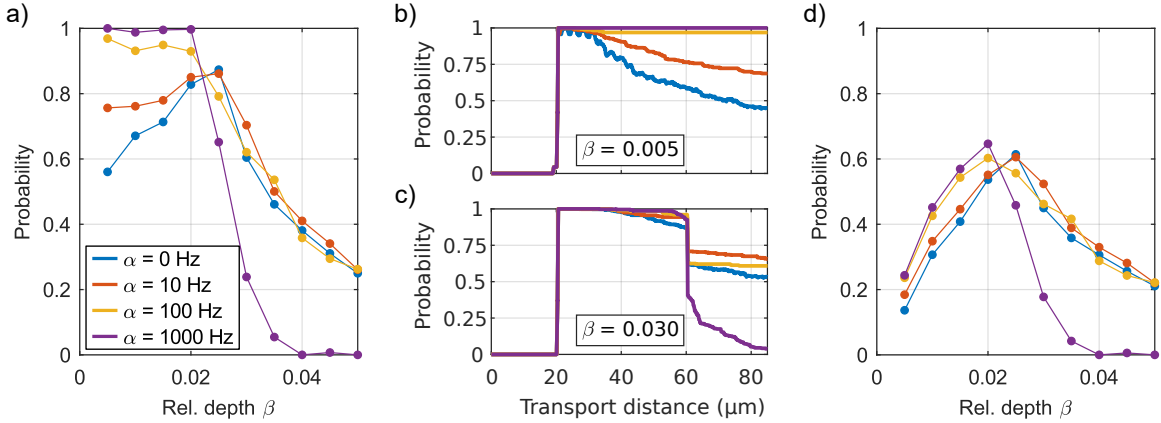


Figure 3.6: a) Drive-through loading as function of the relative depth β with different cooling strength α . The cooling reduces atom losses at low relative depth due to atom recapturing into the lattice and resulting from this transport out of the crossing region. b), c) Traces of $\mathcal{P}(t)$ as function of the transported distance for the same cooling parameters as in a). See the main text for an extended discussion. d) The total drive-through loading probability $\mathcal{P}_{\text{DTL, total}}$ obtained from a) and the atom losses L during transport. A significant fraction of atoms is lost at low relative depth.

overall dependences are preserved, but for slow transport velocities and small relative depths the loading probability increases. The before mentioned influence of the cooling requires a certain duration for the atoms to spend in the cooling region.

The modeling of the cooling as a friction force is a simplified approach in comparison to the degenerate Raman sideband cooling during the transport sequence. In the simulation, the atoms are damped depending on their velocity. Therefore, the modeling is assumed to not yield quantitative result, but help to understand the underlying processes.

Furthermore, the Raman process is tuned to drive transitions between the levels of the harmonic ladder inside the lattice potential wells to reduce the motional quanta of atoms trapped. The actual cooling performance for radial oscillations in the orthogonal trap DT_y relies on non-orthogonality of the optical beams. Hence, the strength of the cooling in the experiment is very hard to estimate.

The results from the simulation reveal a promising technique for loading several atoms into the cavity. The probability for one atom to be loaded from the MOT into the crossed dipole trap peaks at above 60%. If multiple atoms are loaded from the MOT into the lattice, this can result in the accumulation of small atomic ensembles that are coupled to the fiber resonator. The simulation is not involving any particle interaction, which might have an influence on the loading behavior or limit the total number of loaded atoms. The spatial distribution of atoms was not analyzed in the simulation due to its one-dimensional approach. The findings of the simulation are compared to experimental results in the following chapter.

Loading Small Atomic Ensembles into the Cavity

In this chapter, the findings of the numerical simulation for the drive-through loading technique (Chapter 3) are compared to measurement results. Drive-through loading is evaluated in terms of the spatial atom loading distribution by the image analysis described in the first chapter. Furthermore, the comparison of this method to two other loading methods is shown.

4.1 Measurements of Drive-through Loading

First, the experimental sequence to benchmark drive-through loading in terms of the single atom loading probability is described. Afterwards, results from measurements are compared to the previously presented simulation results. In the parameter space of relative depth β , transport velocity v_{tr} and cooling strength α the experimental optimum for the loading probability is given.

4.1.1 Experimental Implementation

The experimental sequence for the implementation of drive-through loading is depicted in Figure 4.1a). After Transport 1, the DT_x lattice is adiabatically lowered with respect to DT_y to a relative depth β . The ramping takes $2\ \mu\text{s}$. Subsequently, the transport continues at velocity v_{tr} until $100\ \mu\text{m}$ behind the cavity. This distance ensures that the MOT distribution, loaded into the dipole trap, has completely gone through and out of the cavity mode. Therefore, atoms present in the cavity after the transport finished are considered to have been loaded by drive-through.

Atoms with high temperatures can escape the trapping potential when the transport lattice is lowered. The lowering happens outside of the cavity and the imaging region, thus the loss of atoms can not be detected until the atoms are transported into the cavity region. There, the presence of an atom can be detected during the full duration of Transport 2 by the cavity-based detection. This yields the probability \mathcal{P}_1 to have at least one atom in the lattice being transported through the cavity from the overall sequence attempts. In the following, this probability is denoted as presence probability $\mathcal{P}_{\text{presence}}$ and the measurement result is shown in Figure 4.1b). A loss of atoms occurs only for relative depth β smaller than 0.1 which indicates that the atoms are loaded with small energies compared to the full trap depth. For relative depth around $\beta = 0.06$, the atoms are additionally heated out of the lattice due to intensity modulation of the lattice beams, which originates from the mode-locking mechanism of the source Ti:Sa laser.

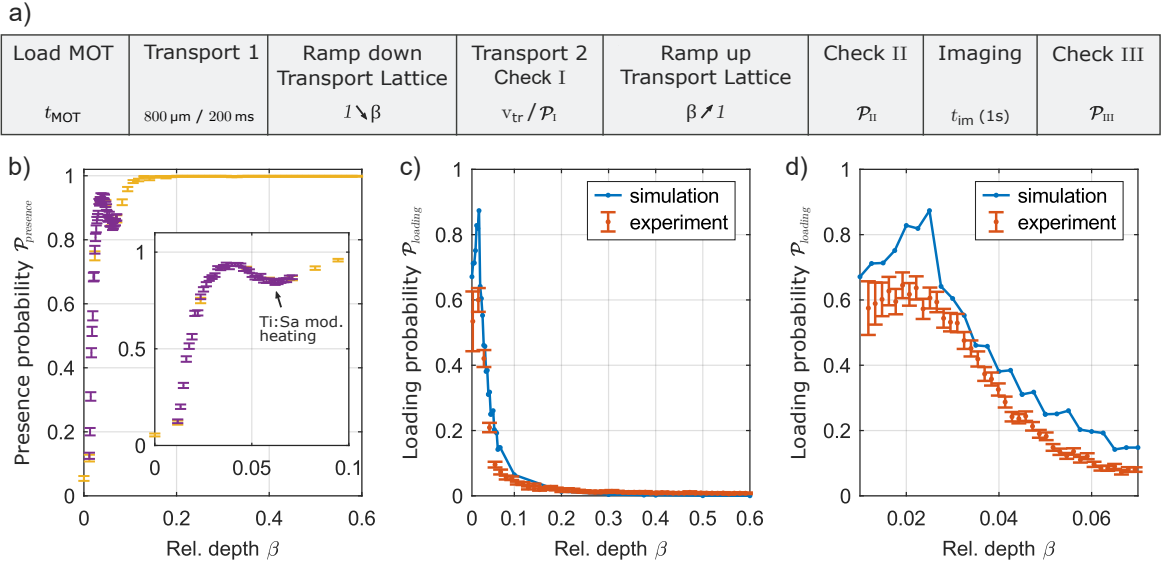


Figure 4.1: a) Experimental sequence for drive-through loading. b) Presence probability as function of the relative lattice depth β for a fine (purple) and coarse (yellow) measurement. Large fraction of atoms escapes the trapping potentials for a shallow depth and are therefore not transported into the cavity. The dip around $\beta = 0.06$, see inset, can be traced back to lattice laser (Ti:Sa) amplitude modulation required for its frequency stabilization. See main text for further details. In addition, the single atom drive-through loading probability obtained from the experiment and the classical 1D simulation (see Chapter 3) is shown for a c) coarse and d) fine sampling of the relative trap depth. The measurement and simulation result are in very good agreement.

The loading sequence is completed by ramping up the transport lattice in $2 \mu\text{s}$ to its full depth. At this point, a second atom check gives a measure of the probability (\mathcal{P}_{II}) to have at least one atom present after the transport finished, compared to the number of total attempts. Our quantity of interest, $\mathcal{P}_{\text{loading}}$, is the single atom loading probability. It can not be computed directly from \mathcal{P}_I and \mathcal{P}_{II} since these quantities are cumulative probabilities $P(n \geq 1)$ for one or more atom. Nevertheless, it can be defined as the ratio of the mean atom number $\lambda_{\text{I,II}}$ present in Check I and Check II, respectively. The mean numbers can be calculated from the check probabilities \mathcal{P}_i , because the number of loaded atoms n is a discrete random variable and follows Poisson statistics. The probability for detecting n atoms is given by

$$P(n) = \frac{\lambda^n e^{-\lambda}}{n!},$$

if the involved processes, here transport and cooling, do not depend on the number of involved atoms. The probability for absence of atoms in the cavity is $P(0) = \exp(-\lambda)$. From this, the mean number of atoms for the atom checks can be calculated as $\lambda_i = -\log(P_i(0)) = -\log(1 - \mathcal{P}_i)$. With this, $\mathcal{P}_{\text{loading}}$ to benchmark the drive-through loading technique is calculated as $\mathcal{P}_{\text{loading}} = \lambda_{\text{II}}/\lambda_{\text{I}}$. After the second atom check, the atoms are imaged for a duration of t_{im} . Another atom presence check is performed to post select images on survival.

4.1.2 Optimization of Atom Loading Probability

The optimization of the single atom loading probability in the experiment follows closely the parameters analyzed in the simulation. The focal point of the transport lattice x_0 is fixed in the experiment and, therefore, only the dependence of $\mathcal{P}_{\text{loading}}$ on the relative depth β , the transport velocity v_{tr} and the effect of cooling during drive-through transport is discussed.

Relative Lattice Depth

In the simulation, the relative depth β of the transport lattice with respect to the orthogonal dipole trap turned out to be the most critical parameter. In Figure 4.1c), the numerical (blue) and the experimental (red) results for the single atom loading probability $\mathcal{P}_{\text{loading}}$ as function of the relative depth are presented. The uncertainties are given as the 68 % confidence intervals. Only for significant lowering of the transport lattice, the atoms are loaded by drive-through. In a small region of low β , the simulation result exceeds 85 % and in the measurement the highest loading probability is $(64.5 \pm 3.9) \%$. The optimum relative trap depth is found to be 0.019 in the measurement as it is shown in the fine parameter scan of β in Figure 4.1d). The qualitative shape of the simulation curve was reasoned in the course of the simulation description (see Chapter 3). The overall lower loading probability obtained in the experiment can be explained by atoms being loaded into the orthogonal trap, but are lost due to heating until the full transport finishes. The experimental result of the single atom loading probability exceeding 60 % is a promising result towards loading multiple atoms with this technique. The absolute number of atoms loaded can be controlled by the MOT loading duration, defining the initial number of atoms inside of the conveyor belt. It has to be noted that the optimum choice for relative depth has to yield high single atom loading probability together with reasonable presence probability. Otherwise, the amount of measurement time increases significantly.

Transport Velocity

The loading probability $\mathcal{P}_{\text{loading}}$ for the parameter scan of the relative depth β and the transport velocity v_{tr} is shown in Figure 4.2a). Different transport velocities are set by the duration in which the atoms are moved by 300 μm . The highest loading probability of $(67.3 \pm 4.0) \%$ is found for $\beta = 0.018$ and $v_{\text{tr}} = 6 \text{ mm/s}$. The measurement results for $\beta > 0.03$ are decreasing qualitative as the simulation results shown in Figure 4.2c). In the simulation, the loading probability peaks around 90 % at low transport velocities (see Chapter 3). The loading probability in the experiment decreases overall for slow transports, because drive-through loaded atoms do not stay in the region of interest until the transport ended. At long transport times, the already loaded atoms have a lot of time to get heated out of the potential.

Effect of Cooling during Drive-through Loading

During Transport 2, the atoms are cooled using degenerate Raman sideband cooling [31]. The cooling can be disabled by switching off a repumper beam, and thereby interrupting the cooling cycle. The single atom loading probability was measured for deactivated cooling and the result is shown in Figure 4.2b), next to the measurement with active cooling in a). Overall, the loading probability decreases and the maximum reduces to $(39.9 \pm 2.3) \%$. The corresponding lowering increases to 0.024 and the velocity is 10 mm/s. The simulation results in Figure 4.2d) match the presented measurement

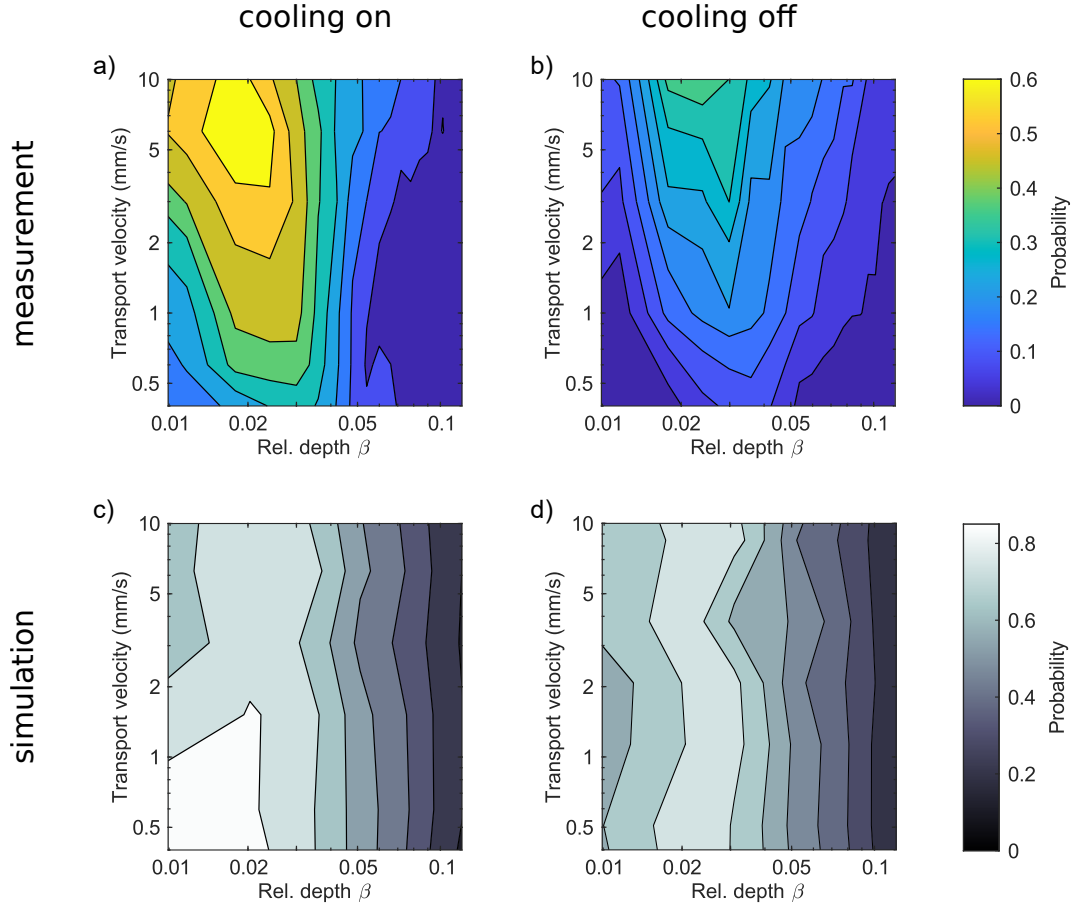


Figure 4.2: Single atom loading probability as function of the relative depth and the transport velocity obtained from measurements, in a) with cooling and b) without cooling, and the simulation, in c) with cooling and d) without cooling. The shapes for the numerical simulation results are discussed in Chapter 3. In a), the loading probability decreases towards slower transports, because atoms loaded by drive-through spend more time in the region of interest until the full transport finishes and are thereby lost in the meantime due to heating. In b), for deactivated cooling during the drive-through transport the atom losses are more significant.

results quantitatively in terms of scaling with the relative depth β . The decrease of loading probability at lower transport velocities is attributed to the increased atom losses due to heating.

4.2 Benchmarking of Three Loading Techniques

In addition to the elaborated drive-through loading, two alternative loading techniques are introduced towards the goal of loading small atomic ensembles. The three methods are analyzed in terms of their atom position distributions within the region of interest.

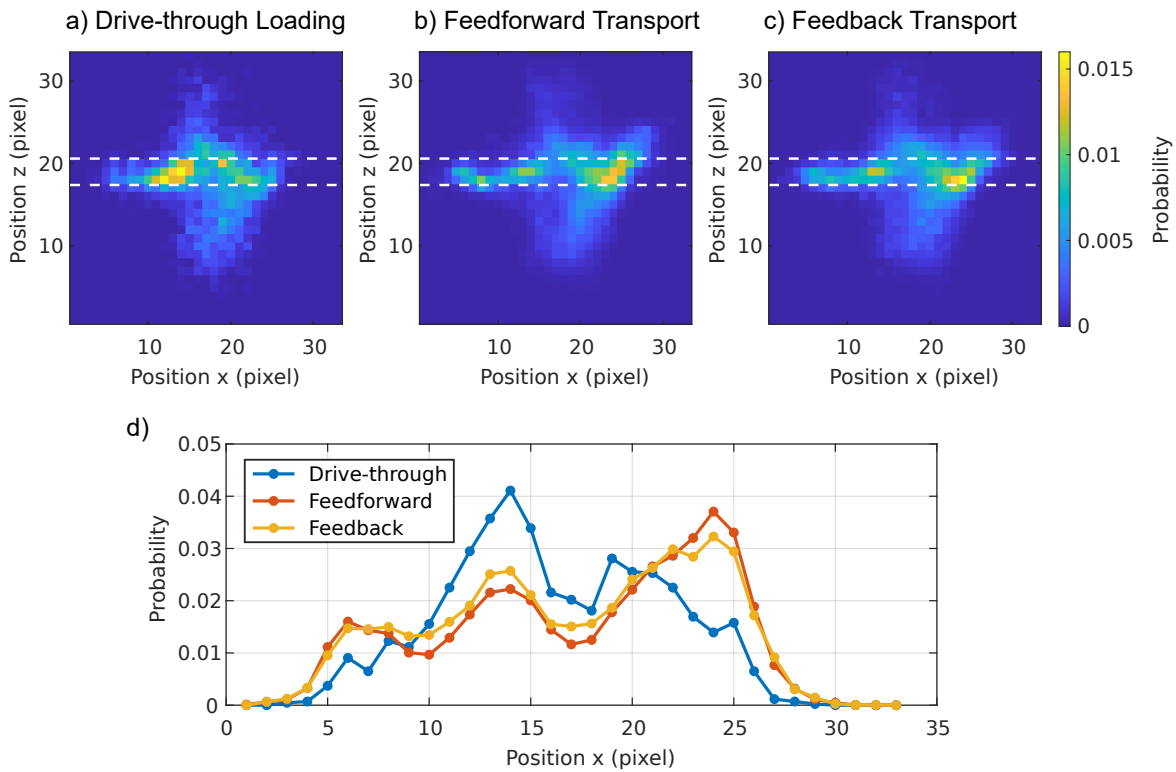


Figure 4.3: The detected peak distributions after a) drive-through loading, b) feedforward transport and c) feedback transport. The distribution integrated along the three indicated z pixels is shown in d). The drive-through loading shows a peak at $x = 14$ pixel which coincides with the center of the orthogonal dipole DT_y . The two alternative loading techniques load atoms into the cavity center located around $x = 24$ pixel.

Two Alternative Loading Techniques

The *feedforward transport* is set up to transport atoms for a fixed distance in order to place the center of the MOT distribution at the cavity center. The *feedback transport* is the second alternative and utilizes the cavity-based atom detection to stop the atom transport conditioned on the detection of the first well coupled atom. This techniques was already introduced and used in Chapter 2.

Compare Spatial Loading Distributions

The three different loading techniques are analyzed in terms of their atom position distributions. This is an important factor as the atoms should be loaded into the center of the cavity. The image analysis for obtaining the peak position distribution was presented in Chapter 2. For this analysis, the images are post selected upon the presence of at least one atom before the picture, but the survival after the picture is not considered. Thereby, atoms can yield lower fluorescence, but their peak position can nevertheless be determined.

For each of the three loading techniques, the peak position distributions are shown in Figure 4.3a)-c). In all three measurements, the MOT was loaded for 100 ms which yields a comparable number of initial atoms in the conveyor belt. For the drive-through loading, the experimentally found optimal

parameters were used. The distribution of atoms along the transport direction (x -axis) determines how well the atoms are located around the cavity center. In Figure 4.3d), the respective integration of the 2D distribution within the indicated z pixel is shown. After drive-through transport, the atoms tend to be located around pixel 14 that coincides with the center of the orthogonal dipole trap DT_y . This confirms the simulation in terms of the underlying effect of atom accumulation in the orthogonal dipole trap potential. The feedforward and feedback loading methods yield the most probable peak position at $x = 24$ pixel, roughly the location of the cavity center. Away from the center, the cooling is less efficient and, therefore, fewer atoms survive and can be imaged. A second peak is at the crossing of DT_y , because there atoms are well trapped in a deeper potential which makes them less susceptible to heating losses. Likewise, a certain fraction of atoms is also detected inside the cavity after drive-through loading as the ones which get into the cavity are well cooled and detected. The mismatch of 10 pixel corresponds to about $4.6 \mu\text{m}$. The observed double peak feature in the position distributions hampers the direct comparison of atom spread around the cavity center for the three different loading techniques. After the overlapping of the orthogonal trapping beam with cavity, it is assumed that the distribution of atoms loaded by drive-through peaks at around $x = 24$ pixel. Furthermore, it is expected that the resulting distribution is narrower than the ones from the alternative methods. Wherein, the peak around pixel 14 is expected to get overlapped with the cavity location, but, nevertheless, atoms will still be loaded with a larger spread due to the width of the MOT distribution loaded into the conveyor belt.

The mean number of detected peaks per image μ_{peaks} is calculated for the three different loading techniques as:

	Drive-through Loading	Feedforward Transport	Feedback Transport
μ_{peaks}	0.7	2.8	2.3

The lower mean number of detected peaks for the drive-through loading could be caused by the fact that the Raman cooling is not optimized for the position around the orthogonal trap center and, thereby, the atoms do not survive long enough to yield sufficient fluorescence to be detected in the image analysis. For all the three techniques, mean numbers can be scaled with the duration of the MOT loading. For the feedforward and feedback transport, involving the positioning the MOT distribution with respect to the cavity, the atoms are broadly distributed around the cavity. The drive-through loading has the possibility to load multiple atoms centered around the orthogonal dipole trap and, for the realigned system, centered in the cavity.

Discussion and Outlook

In this thesis, I presented the preparation and detection of small atomic ensembles in a fiber cavity. First, I introduced the sequence to perform Raman imaging cooling with which we record fluorescence images of atoms inside the cavity. Then, I implemented an algorithm to determine the position of atoms with sub-pixel resolution. The position distribution was used to reconstruct the optical lattice inside of our fiber cavity. Towards the goal of counting atoms, I developed an algorithm that adaptively integrates the fluorescence in a local neighborhood around the detected position of atoms. Against our expectations, the obtained fluorescence histograms did not allow us to determine the number of atoms in an image deterministically. However, an unexpected result was to learn from the image analysis that our system suffers from a highly inhomogeneous atom fluorescence distribution, correlated to the atom positions inside the cavity. This might be the main cause of the broadening of the fluorescence histogram that we observed. Furthermore, by extracting the atom position distribution independent from the fluorescence, we gained new insight into the geometry of our lattices and the atom loading process.

In the second chapter, I investigated a novel atom loading technique by drive-through transport: the empirically observed effect of the atoms remaining at the orthogonal lattice crossing when transported through with the conveyor belt. The classical 1D simulation helped to understand the process of atoms escaping their transport lattice sites upon entering the potential of an orthogonal dipole trap. The relative depth between the two traps was found to be the most important parameter. The transport velocity and the possibility of cooling during transport are possible tuning parameters in the experiment and that were also investigated in the simulation. At the optimum settings, the simulation predicts a single atom loading probability exceeding 80%. The atom number probabilities for loading simultaneously into the cavity can be tuned by the initial number of atoms loaded from the MOT to the conveyor belt.

Following the results from the simulation, the drive-through loading was measured in the experiment. The obtained single atom loading probabilities, probed at various relative depths, are in very good agreement with the simulation. By performing scans of the transport velocity, we found that the atoms are susceptible to heating during the drive-through transport. This is mainly because at low transport velocities the atoms spend more time subject to heating processes. The heating losses are compensated by applying cooling during the transport and, thereby, single atom loading probabilities of up to 67 %

were observed. For the optimized drive-through loading, we recorded fluorescence images from which the atom position distribution was obtained via processing the image as described in the first chapter. We found that the orthogonal dipole trap is not properly overlapped with the center of the cavity mode. The drive-through loaded atoms have a lower survival probability and their imaging does not work properly. As a consequence, the characterization of the loaded atom numbers is not yet possible. The center of the cavity is $\sim 4.5 \mu\text{m}$ displaced from the orthogonal trap. We plan to eliminate this mismatch by realigning the orthogonal dipole trap beams. Thereafter, the drive-through loading is assumed to be a promising candidate to load atomic ensembles into the cavity center. The resulting spread of atoms along the transport axis can be smaller than the initial atom distribution, given by the loading of the MOT into the conveyor belt. Furthermore, after comparison with two alternative more conventional loading techniques, we conclude that the loading density achieved by the new technique can be higher.

In order to be able to perform experiments with multiple atoms, a better determination of atoms inside the cavity is still to be achieved. So far, the inhomogeneous fluorescence distribution still prevents us from counting the atoms. As a possible solution, we plan to adapt the technique of selective parametric heating of atoms presented by Regal *et al.* [35]. The method that we propose involves amplitude modulation of the intra-cavity lattice to heat atoms out of the trapping potential depending on their radial position with respect to the cavity center. The atoms have different trapping frequencies depending on their radial position and the selection radius can be controlled by the modulation frequency. This would possibly allow us to reduce the width of the atom loading distribution, resulting in a more homogeneous fluorescence needed for counting atoms, and a better coupling of small atomic ensembles to the cavity.

Bibliography

- [1] T. H. Maiman, “Stimulated Optical Radiation in Ruby”, *Nature* **187** (1960) 493 (cit. on p. 1).
- [2] J. A. Jones and M. Mosca,
“Implementation of a quantum algorithm on a nuclear magnetic resonance quantum computer”,
The Journal of Chemical Physics **109** (1998) 1648 (cit. on p. 1).
- [3] I. L. Chuang et al., “Experimental realization of a quantum algorithm”, *Nature* **393** (1998) 143
(cit. on p. 1).
- [4] S. Gulde et al.,
“Implementation of the Deutsch–Jozsa algorithm on an ion-trap quantum computer”,
Nature **421** (2003) 48 (cit. on p. 1).
- [5] A. K. Ekert, “Quantum cryptography based on Bell’s theorem”,
Phys. Rev. Lett. **67** (6 1991) 661 (cit. on p. 1).
- [6] C. H. Bennett et al., “Experimental quantum cryptography”, *Journal of Cryptology* **5** (1992) 3,
URL: <https://doi.org/10.1007/bf00191318> (cit. on p. 1).
- [7] T. Jennewein et al., “Quantum Cryptography with Entangled Photons”,
Phys. Rev. Lett. **84** (20 2000) 4729 (cit. on p. 1).
- [8] H. J. Kimble, “The quantum internet”, *Nature* **453** (2008) 1023 (cit. on p. 1).
- [9] J. I. Cirac et al., “Quantum State Transfer and Entanglement Distribution among Distant Nodes
in a Quantum Network”, *Physical Review Letters* **78** (1997) 3221 (cit. on p. 1).
- [10] L. Luo et al., “Protocols and techniques for a scalable atom-photon quantum network”,
Fortschritte der Physik **57** (2009) 1133 (cit. on p. 1).
- [11] W. K. Wootters and W. H. Zurek, “A single quantum cannot be cloned”, *Nature* **299** (1982) 802
(cit. on p. 1).
- [12] C. H. Bennett et al., “Teleporting an unknown quantum state via dual classical and
Einstein-Podolsky-Rosen channels”, *Physical Review Letters* **70** (1993) 1895,
URL: <https://doi.org/10.1103/physrevlett.70.1895> (cit. on p. 1).
- [13] H.-J. Briegel et al.,
“Quantum Repeaters: The Role of Imperfect Local Operations in Quantum Communication”,
Physical Review Letters **81** (1998) 5932,
URL: <https://doi.org/10.1103/physrevlett.81.5932> (cit. on p. 1).
- [14] M. Körber et al., “Decoherence-protected memory for a single-photon qubit”,
Nature Photonics **12** (2017) 18 (cit. on p. 1).
- [15] J. Huwer et al., “Photon entanglement detection by a single atom”,
New Journal of Physics **15** (2013) 025033 (cit. on p. 1).

- [16] C. Kupchak et al., “Room-Temperature Single-photon level Memory for Polarization States”, *Scientific Reports* **5** (2015) (cit. on p. 1).
- [17] Y.-W. Cho et al., “Highly efficient optical quantum memory with long coherence time in cold atoms”, *Optica* **3** (2016) 100 (cit. on p. 1).
- [18] M. Sabooni et al., “Efficient Quantum Memory Using a Weakly Absorbing Sample”, *Physical Review Letters* **110** (2013) (cit. on p. 1).
- [19] A. I. Lvovsky, B. C. Sanders and W. Tittel, “Optical quantum memory”, *Nature Photonics* **3** (2009) 706 (cit. on p. 1).
- [20] D. Hunger et al., “A fiber Fabry–Perot cavity with high finesse”, *New Journal of Physics* **12** (2010) 065038 (cit. on p. 1).
- [21] A. D. Boozer et al., “Reversible State Transfer between Light and a Single Trapped Atom”, *Physical Review Letters* **98** (2007) (cit. on p. 1).
- [22] L. Giannelli et al., “Optimal storage of a single photon by a single intra-cavity atom”, *New Journal of Physics* **20** (2018) 105009 (cit. on p. 1).
- [23] R. J. Thompson, G. Rempe and H. J. Kimble, “Observation of normal-mode splitting for an atom in an optical cavity”, *Physical Review Letters* **68** (1992) 1132 (cit. on p. 1).
- [24] W. Petrich et al., “Behavior of atoms in a compressed magneto-optical trap”, *J. Opt. Soc. Am. B* **11** (1994) 1332 (cit. on pp. 1, 18).
- [25] R. Grimm, M. Weidemüller and Y. B. Ovchinnikov, “Optical Dipole Traps for Neutral Atoms”, ed. by B. Bederson and H. Walther, vol. 42, *Advances In Atomic, Molecular, and Optical Physics*, Academic Press, 2000 95, URL: <http://www.sciencedirect.com/science/article/pii/S1049250X0860186X> (cit. on pp. 1, 20).
- [26] S. Kuhr, “Deterministic Delivery of a Single Atom”, *Science* **293** (2001) 278 (cit. on pp. 1, 4).
- [27] Y. Colombe et al., “Strong atom–field coupling for Bose–Einstein condensates in an optical cavity on a chip”, *Nature* **450** (2007) 272 (cit. on p. 1).
- [28] I. Bloch, J. Dalibard and W. Zwerger, “Many-body physics with ultracold gases”, *Rev. Mod. Phys.* **80** (3 2008) 885 (cit. on p. 1).
- [29] D. Schrader et al., “An optical conveyor belt for single neutral atoms”, *Applied Physics B* **73** (2001) 819 (cit. on pp. 1, 4).
- [30] V. Vuletić et al., “Degenerate Raman Sideband Cooling of Trapped Cesium Atoms at Very High Atomic Densities”, *Physical Review Letters* **81** (1998) 5768 (cit. on p. 2).
- [31] E. Uruñuela et al., “Ground-state cooling of a single atom inside a high-bandwidth cavity”, *Physical Review A* **101** (2020) (cit. on pp. 2, 6, 31).
- [32] R. Reimann et al., “Carrier-free Raman manipulation of trapped neutral atoms”, *New Journal of Physics* **16** (2014) 113042 (cit. on p. 2).

-
- [33] J. Gallego et al., “Strong Purcell Effect on a Neutral Atom Trapped in an Open Fiber Cavity”, *Phys. Rev. Lett.* **121** (17 2018) 173603 (cit. on p. 2).
- [34] T. Macha et al., “Nonadiabatic storage of short light pulses in an atom-cavity system”, *Phys. Rev. A* **101** (5 2020) 053406 (cit. on p. 2).
- [35] B. J. Lester, A. M. Kaufman and C. A. Regal, “Raman cooling imaging: Detecting single atoms near their ground state of motion”, *Phys. Rev. A* **90** (1 2014) 011804 (cit. on pp. 2, 6, 36).
- [36] J. C. Gallego Fernández, “Strong Coupling between Small Atomic Ensembles and an Open Fiber Cavity”, PhD thesis, University of Bonn (2017) (cit. on pp. 3–6, 18, 41, 49).
- [37] E. Uruñuela, “Imaging and addressing of neutral atoms inside a fiber cavity”, Master thesis, University of Bonn (2017) (cit. on pp. 3, 7).
- [38] R. W. P. Drever et al., “Laser phase and frequency stabilization using an optical resonator”, *Applied Physics B Photophysics and Laser Chemistry* **31** (1983) 97 (cit. on p. 3).
- [39] W. D. Phillips and H. Metcalf, “Laser Deceleration of an Atomic Beam”, *Physical Review Letters* **48** (1982) 596 (cit. on p. 3).
- [40] E. L. Raab et al., “Trapping of Neutral Sodium Atoms with Radiation Pressure”, *Physical Review Letters* **59** (1987) 2631 (cit. on p. 3).
- [41] T. Macha, “Storage of Short Light Pulses in a Fiber–Based Atom–Cavity System”, PhD thesis, University of Bonn (2018) (cit. on p. 4).
- [42] J. Goldwin et al., “Fast cavity-enhanced atom detection with low noise and high fidelity”, *Nature Communications* **2** (2011) (cit. on p. 4).
- [43] P. Malik, “Linewidth-reduced DBR Laser for Raman Sideband Cooling”, Master thesis, University of Bonn (2020) (cit. on pp. 6, 7).
- [44] M. Ammenwerth, “Raman Imaging of Small Atomic Ensembles Inside an Optical Cavity”, Master thesis, University of Bonn (2020) (cit. on pp. 6–8).
- [45] M. Karski, “State-selective transport of single neutral atoms”, PhD thesis, University of Bonn (2010) (cit. on pp. 10–12).
- [46] A. Neuzner, “Resonance Fluorescence of an Atom Pair in an Optical Resonator”, PhD thesis, Technical University of Munich (2016) (cit. on pp. 11, 12).
- [47] W. Williams and M. Saffman, “Compression and localization of an atomic cloud in a time dependent optical lattice”, *Journal of Modern Optics* **55** (2008) 2187 (cit. on p. 17).
- [48] M. T. DePue et al., “Unity Occupation of Sites in a 3D Optical Lattice”, *Phys. Rev. Lett.* **82** (11 1999) 2262 (cit. on p. 18).
- [49] C. Cohen-Tannoudji, J. Dupont-Roc and G. Grynberg, *Atom—Photon Interactions*, Wiley, 1998 (cit. on p. 19).
- [50] D. J. Wineland and W. M. Itano, “Laser cooling of atoms”, *Phys. Rev. A* **20** (4 1979) 1521 (cit. on p. 19).

- [51] L. F. Shampine, I. Gladwell and S. Thompson, *Solving ODEs with MATLAB*, Cambridge University Press, 2003, ISBN: 9780521824040, URL: <https://www.cambridge.org/de/academic/subjects/mathematics/numerical-analysis/solving-odes-matlab?format=HB&isbn=9780521824040> (cit. on p. 21).
- [52] W. Alt, “Optical control of single neutral atoms”, PhD thesis, University of Bonn (2004) (cit. on p. 23).
- [53] M. M. Dorantes, “Fast non-destructive internal state detection of neutral atoms in optical potentials”, PhD thesis, University of Bonn (2016) (cit. on p. 41).
- [54] B. Brandstätter et al., “Integrated fiber-mirror ion trap for strong ion-cavity coupling”, *Review of Scientific Instruments* **84** (2013) 123104 (cit. on p. 49).
- [55] D. Gangloff et al., “Preventing and reversing vacuum-induced optical losses in high-finesse tantalum (V) oxide mirror coatings”, *Optics Express* **23** (2015) 18014, URL: <https://doi.org/10.1364/oe.23.018014> (cit. on p. 49).
- [56] T. G. Ballance et al., “Cavity-induced backaction in Purcell-enhanced photon emission of a single ion in an ultraviolet fiber cavity”, *Physical Review A* **95** (2017), URL: <https://doi.org/10.1103/physreva.95.033812> (cit. on p. 49).

Assembly of a High-NA Imaging System

In our experiment, the cavity is placed in the center of four high NA lenses. The focal points of the four lenses overlap. The first set of lenses was built by M. Dorantes [53] and it was improved and combined with the fiber cavity by J. Gallego [36]. It was planned to build a full back-up for the current experiment setup, consisting of the fiber cavity and the lens system. The assembly of the four lenses was done in the course of an internship before this thesis and parts of the report are given here.

The structure of this report is based on the steps I followed to build the final set of lenses. For the alignment of the four high-NA lenses, 780 nm light was used to keep aberrations low as this light is used especially in the photon storage experiments. As this lens system is meant to be placed under ultra-high vacuum, all the parts of the system are needed to be cleaned with isopropyl or acetone alcohol and in an ultrasonic bath to make the system vacuum compatible.

High NA Lenses

The heart of the system are four small aspheric lenses (Thorlabs 354240-B, $f = 8.0$ mm) with $NA = 0.5$. They are used to focus the laser beams, e.g. for the dipole trap, at the cavity center and collect the free-space emission of the atoms. Due to the in-vacuum placement high pointing stability and efficient collection of free-space emission is achieved. The high NA lenses are made for laser diode collimation and are typically mounted in a housing with an output window, so during the alignment procedure compensation lenses (Thorlabs LA1464-B, $f = 1000$ mm) are used to mimic the windows. A sketch of a high NA lens is shown in Figure A.1(b).

Grinding the Lenses

The optical access for the MOT beams in the experiment setup is guaranteed by grinding the lenses with different depth. The top view of this configuration is shown in Figure A.1(a). The two depth values can be seen in Figure A.1(b). A self-made holder, see Figure A.1(c) and (d), is used to grind two different depth into the lenses. The grind depth is adjusted by the two outer aluminum bars. In this holder a lens is fixed with thermal wax (Nikka Seiko Shiftwax 582W) to avoid moving of the lens during grinding. To remove the lens from the holder, the wax is heated up with a heat gun. After grinding the wax is removed with isopropyl alcohol. For the grinding sandpaper with a grain of 150 is

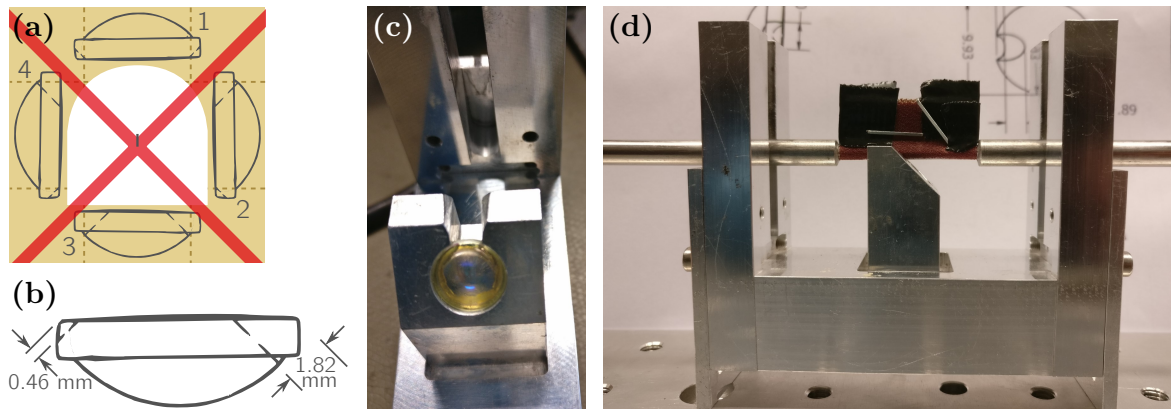


Figure A.1: (a) Schematic of the MACOR holder with four indicated deepenings for the lenses. In addition the grinding depth for each lens is indicated. In black the sphere is shown in the center of the holder and the two red MOT beams overlap 1 mm away from the sphere. (b) Sketch of a high NA lens and the two different required grind depths. (c, d) Self-made holder to grind a lens to different depths. The lens is fixed in the holder with wax. The grinding depth is defined by the two outer sliders which are fixed with screws. The grind diameter should be around 2.8 mm and hence the sandpaper on the rod should not exceed this in diameter.

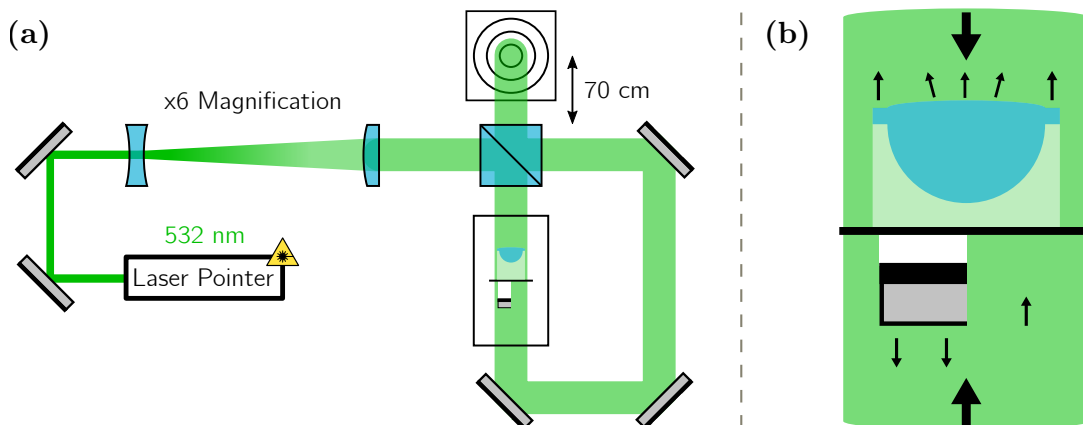


Figure A.2: Interferometer with a 532 nm laser. (a) Optical setup. (b) Reflection from outer rim of the lens creates a ring on the target. Orientation of the half-mirror is adjusted such that its reflection mirrors its relative position to the optical beam on the target. For more details see Fig A.3(c)-(g).

mounted on a self-made rod. The grindings in the lens should not be too wide, so the diameter of the sandpaper around the rod should not exceed 2.8 mm. For further details take a look at Figure A.7(a).

Parallel Alignment of Lens and Half-Mirror

The high NA lenses in the final assembly have to be aligned with high accuracy as in Figure A.1(a). Lens 1 and 3 need to be parallel wrt each other as well as lens 2 and 4. These two lens pairs have to be perpendicular to each other as well as the focal points of all four lenses coincide. The alignment is done with a 780 nm laser and the back reflection from the lens would be well suited to position the lens correct. The high NA lenses have an anti-reflection coating for this wavelength and hence a

different technique is required. We use a half-mirror which will be aligned parallel to the lens. In the final assembly the mirror will be aligned to be perpendicular to the beam and therefore the lens will be perpendicular as well. The holder configuration is shown in Figure A.3(a, b). The holder is mounted on a 3D translation stage. In general one has to take spherical aberrations into account and therefore the curved surface of the lens should be oriented towards the incoming beam. The lens is fixed with a 3D printed piece of plastic. To parallelize the lens and the mirror the interferometer shown in Figure A.2(a) is used. The interference ensures that the beams counter-propagate within the interferometer and they can be used to align the lens and the mirror.

A green laser pointer at 532 nm is magnified. The beam has to cover the lens to use the lens rim reflection for alignment. Compare with Figure A.2(b). The interferometer is built by a beamsplitter and three mirrors. The interfering beam is impinging onto a target (see photo in Figure A.3(c)). The lens-mirror configuration is placed in the interferometer where the beams are counter-propagating. The reflected beams from the lens and the mirror are used to reference their relative orientation. A schematic of the lens and mirror reflection is depicted in Figure A.2(b). Due to the fact that only reflections are of interest, the transmission is blocked by a piece of paper between the lens and the mirror.

The misaligned lens rim and half-mirror reflection can be seen in Figure A.3(d). The deeper grindings can be seen in the reflection. For this specific lens only one grinding is visible. This should be horizontally symmetric to ensure that the lens rotation is correct. The lens reflection is centered on the target by adjusting the red Thorlabs mount (e). The mirror reflection is moved independently from the lens with the smaller black mount until it is within the inner ring of the target, see (f). Its position should reproduce the cut-out that is visible in the transmission behind the mirror, see (g). After the alignment steps the lens and the mirror are perpendicular to each other and can be placed in the main interferometer.

Lens Placement and Gluing to Mount

For the alignment of the four lenses with respect to each other the interferometer shown in Figure A.4(a) is used. A 780 nm laser in single-mode operation, which is required to use interference for alignment, is used. First the laser is coupled out from coupler C1 to use a small beam for alignment. The coupler mount and the flip mirror mount are used to align the beam such that it follows a line of holes on the optical table. A beam profile camera (BPC) with a fixed height is screwed along a line of holes and is used to reference the beam path. The camera on the mount is shown in Figure A.4(b). The BPC camera is used to reference the beam to the table holes. After the first mirror is aligned the lower left mirror is aligned in the same way. Thereafter all elements in clockwise direction are aligned one after the other. The last element placed is BS 1 and the whole interferometer is setup correct if the beam on the left output of BS 1 is showing interference. Interference should also be present on the beams exiting BS 2 at the bottom and BS 3 to the right. The outputs can be checked on the BPC at the two indicated positions. There the camera is mounted such that it can be swapped between the two positions and keep its position and orientation for reference.

After aligning the optical elements the laser is coupled out of coupler C2 and is magnified in a telescope by a factor of 4. Subsequently it is split up at BS 1, 2 and 3 to have four beams overlapping at the center of the interferometer. This center is defined as the later joint focal point of the four high

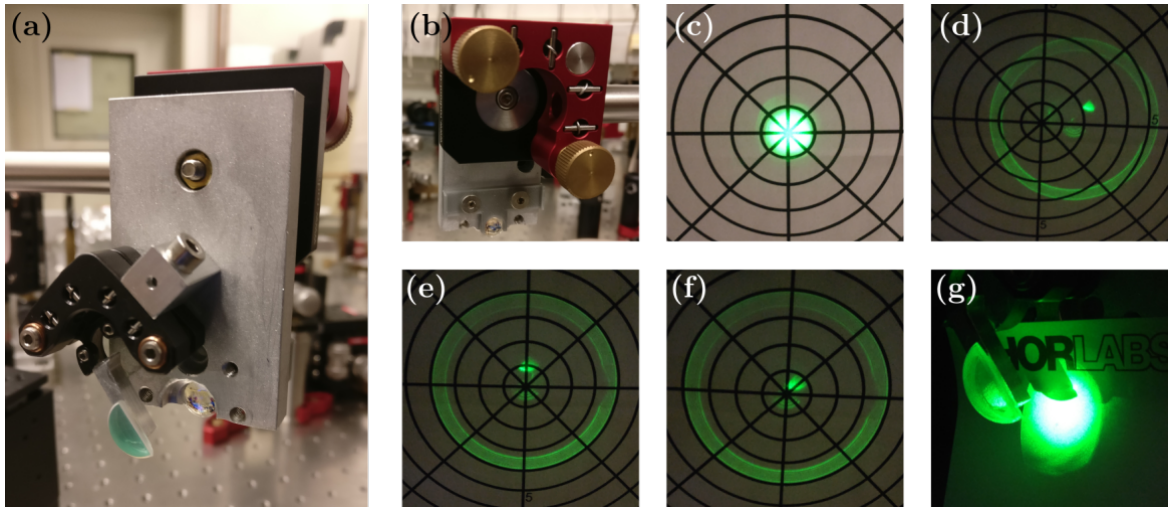


Figure A.3: **(a)** Self-made holder for a lens and a half-mirror. The mirror orientation can be independently adjusted with respect to the lens orientation. **(b)** The grindings has to be horizontally oriented. The free-hanging lower part of the lens is later glued to a holder. **(c)** An interfering beam impinging onto a target behind the output of the 532 nm interferometer. The beam is centered on the target and matched to the first ring in size. **(d)** The holder with lens and half-mirror is inserted into the setup and the mount is roughly positioned such that both reflections are visible on the target. **(e)** By adjusting the red Thorlabs mount the bigger ring from the lens rim reflection is centered. **(f)** The mirror reflection is positioned by adjusting the black mount. It should impinge in the inner target ring and match the beam fraction which is reflected by the half-mirror. **(g)** Indicate the reflected fraction of the beam by the half-mirror.

NA lenses and marked by a ceramic sphere¹. At this point the overlap of all four beams should be maximal. The beam alignment relative to the sphere is optimized until the shadow of the sphere looks like in Figure A.5(a) for each of the four beams. The beams passing out of BS 2 and 3 are aligned onto the BPC and their position on the camera image is marked for later reference. Compensation lenses, as mentioned in Section A, are placed 443 mm away from the center of the interferometer. Before and after placing the compensation lenses, the beam on the target should be at the same position. By that the compensation lenses are centered and parallel wrt the beam. The compensation lenses are plano-convex and create a dim circular interference pattern. This pattern is symmetric around the target center, if the lens is centered and perpendicular to the beam. An exemplary interference pattern is shown in the appendix in Figure A.7(b).

The following explanation will describe the placement of a lens in beam 1 and the placement of the other three lenses can be done in similar way. The lens-mirror combination is placed in the beam such that the mirror reflects beam 1 and the reflection is monitored on the BPC, as shown in a screenshot from the camera software in Figure A.5(b). The mirror reflection has to match to the reference position marked on the BPC. The mirror reflection is smaller than the collimated beam, because the compensation lens focuses it onto the camera. For the alignment of the high NA lens the mirror is partially covered, because its reflection would hide the low intensity sphere reflection. This sphere reflection is the reflected beam from the sphere surface and is created if the high NA lens focuses the incoming beam into the sphere center. In this case the wavefronts of the beam match the

¹ Made by Saphirwerk with a surface roughness of $0.01 \mu\text{m}$ (class G3)

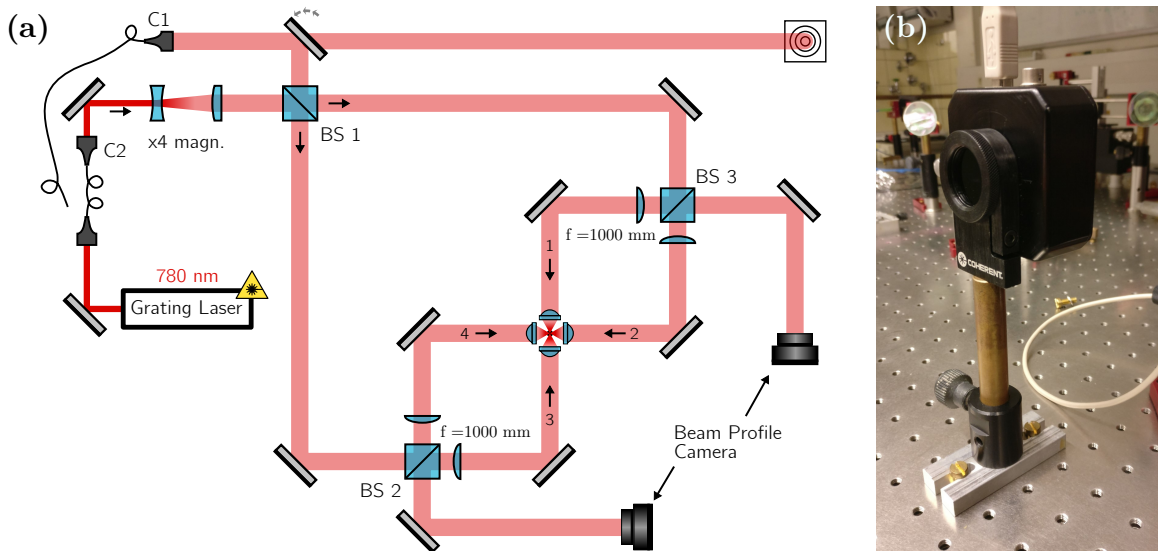


Figure A.4: **(a)** Main interferometer with a 780 nm laser. The laser beam is expanded in a x4 telescope and split up by three beam splitters into four beams. These four beams are guided to intersect at a reference position marked by a ceramic sphere. The beam pairs 1 – 3 and 2 – 4 counter propagate and each adjacent beam pair is perpendicular. These beams are used to reference the positioning of the four high NA lenses to have a joint focal point. For further explanation see text. **(b)** Beam profile camera mounting which was used to align the interferometer. For easier alignment the beam path has to coincide with lines of holes on the optical table.

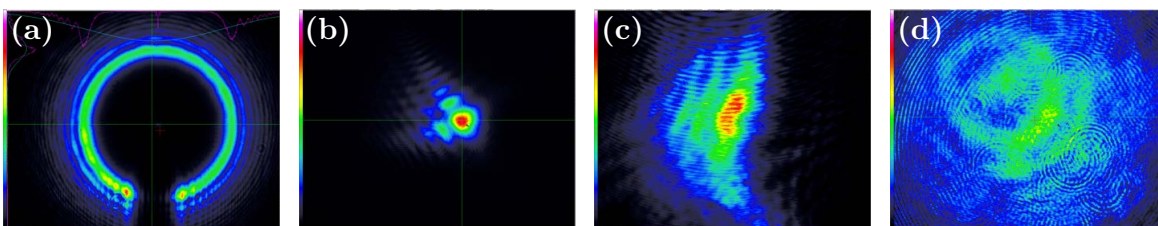


Figure A.5: Screenshots from the beam profile camera software. The beam power was adjusted between images to optimize the contrast. **(a)** Shadow of the sphere in one of the beam paths. **(b)** Reflection from the half-mirror. It appears small, because the beam passes two times through the compensation lenses. It is roughly centered by moving the holder and adjusting the red Thorlabs mount. Afterwards the mirror has to be partially covered with black aluminum foil, because its reflection has more intensity than the sphere reflection. **(c)** Beam reflection from the sphere, created by focusing the laser with the high NA lenses into the sphere center. The collimation and pointing on the BPC can be adjusted with a translation stage. The missing intensity on the right is blocked by the half-mirror. **(d)** After gluing and removing the half-mirror the full reflection from the sphere is visible.

radius of curvature of the sphere and the light is retro-reflected as shown in Figure A.8(a). One has to be careful to not mix up the retro-reflection with the reflection from the sphere surface. Compare Figure A.8(a) and (b). The lens position is adjusted until the beam is retro-reflected and collimated in front of the BPC. The collimation is checked with a Shearing-Interferometer and optimized by axial displacement. The beam on the BPC relative to the marked reference, like in Figure A.5(c), helps to adjust the radial lens positioning. The visible missing part of the beam is cut out by the half-mirror. The lens is well aligned if the beam on the camera looks similar to A.5(c).

The next step is to glue the lens to a holder. This holder was installed during the alignment of the setup and is made out of MACOR². This material is vacuum compatible and can be processed in the institute workshop. The design for the complete holder set was designed by J. Gallego and the full sketch can be found in his thesis. The lower part of the holder is depicted in Figure A.6(a) and (b) and the top part is shown in (e). The lower part of the holder is fixed in a self-made mount and installed on a translation stage in the setup. For the first lens the holder can be completely moved down to the limit of the holder translation stage. For all other lenses the holder should not be moved again, because otherwise one loses the reference on the camera and hence the relative height between the lenses is wrong. Instead the lenses are moved up to make it easier to put the glue onto the holder. The lenses are glued with UV curing vacuum compatible glue³. The glue is put to the holder with the tip of a syringe. The lens position is referenced during the gluing process by the BPC image. The glue is cured with a UV LED⁴ which is collimated with a $f = 25$ mm lens.

The alignment procedure is repeated three more times for the other lenses. After gluing the last lens the beam reflections from the sphere of all four beams can be checked on the BPC. This ensures that all four lenses are well aligned before continuing with the installation of the fiber-cavity.

Outlook

The four high NA lenses in the FCQED experiment are focusing into the center of a fiber-based micro cavity. We plan to build a backup cavity and combine it with the lens-system to have a full backup for the science vacuum chamber for the main experiment.

² Corning, MACOR[®] Machinable Glass, <http://www.corning.com/emea/de/products/advanced-optics/product-materials/specialty-glass-and-glass-ceramics/glass-ceramics/macor.html>

³ EPO-TEK OG116-31

⁴ Thorlabs M365LP1 (4V, 1.7A), connected with Thorlabs CON8ML-4

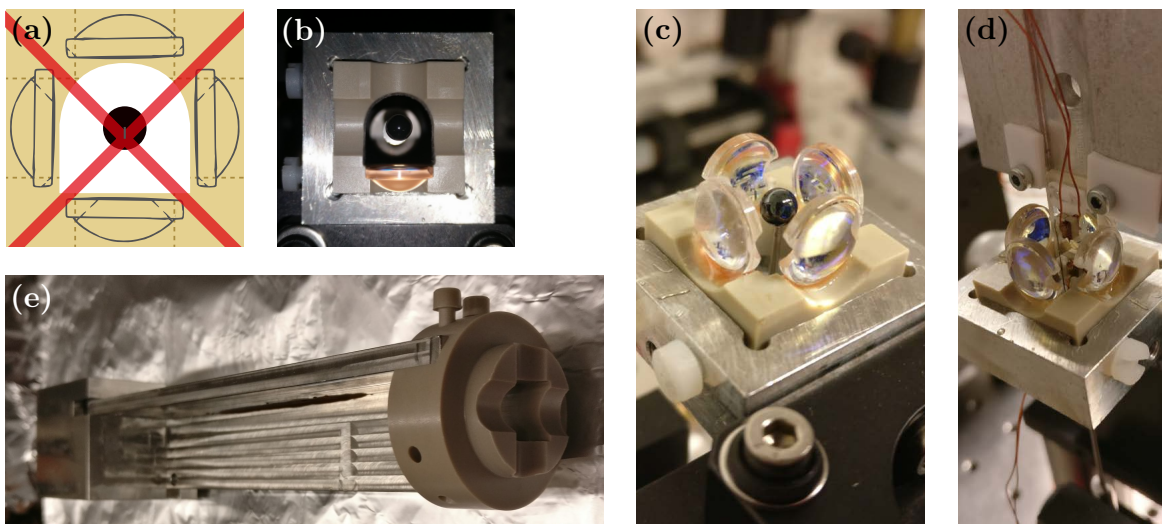


Figure A.6: **(a)** Schematic of the MACOR holder with four indicated deepenings for the lenses. In addition the grinding depth for each lens is shown, if the cavity base plate is glued to the inner flat surface of the holder. In black the sphere is shown in the center of the holder and the two red MOT beams overlap 1 mm away from the sphere. **(b)** MACOR holder with one glued high NA lens and the ceramic reference sphere. **(c)** Four glued test lenses with incorrect grindings. **(d)** Test cavity mounted on a self-made holder and already placed within the lens holder. Its position can be adjusted by a 3D translation stage. **(e)** The MACOR piece on the right is glued to the top of the lenses after the cavity is installed. Two aluminum bars are glued to each other and fixed with MACOR plugs to mount the assembly in a vacuum chamber.

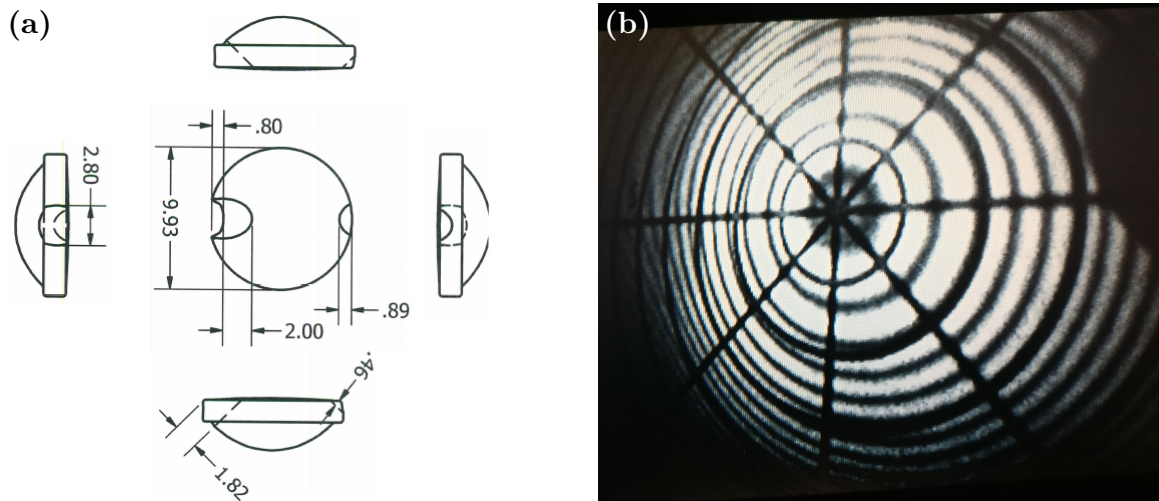


Figure A.7: **(a)** Schematic of the grindings in the high NA lenses. **(b)** Photo of the beam passing out of BS 1 and impinging on the target. The interference fringes originate from the fact that the lens is plano-convex and the beam is partially reflected on the two lens surfaces. The pattern is used to reference the positioning of the compensation lenses.

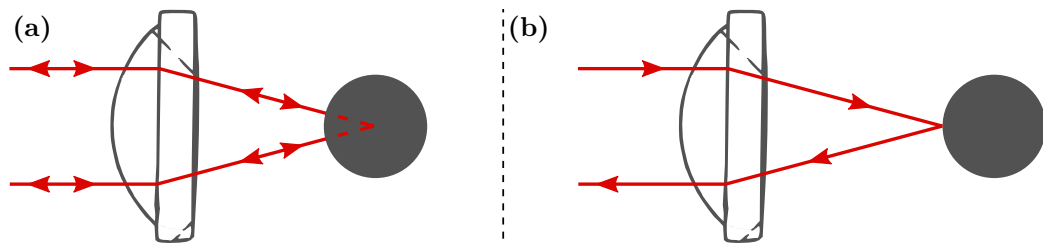


Figure A.8: Schematic of the sphere reflections. **(a)** The high NA lens focuses the beam into the center of the sphere. The beam wavefront curvature matches the sphere radius and therefore the beam gets retro-reflected. **(b)** The beam is focused onto the sphere surface and the beam is reflected. It is possible to distinguish by the two cases by blocking the beam from one radial direction. The blocking direction should match the blocked portion of the beam on the BPC.

Monitoring Vacuum Pressure and Cavity Finesse

The pressure inside the vacuum chamber had been monitored over the course of this work and is shown in Figure B.1a). A rise in pressure over time was already reported by J. Gallego [36]. Furthermore, the reduction of the cavity finesse is mentioned to occur alongside the pressure rise. Over the last year, the finesse was monitored (see Figure B.1b)). The decrease in finesse is attributed to a degradation of the optical coating of the high-reflectivity cavity mirrors as it has been observed in other experiments [54–56]. The finesse can be recovered by filling the vacuum chamber with oxygen. This treatment was done in August 2019 and the finesse was recovered to 28 800. After pumping to ultra-high vacuum, the background vapor is reestablished by heating a rubidium reservoir.

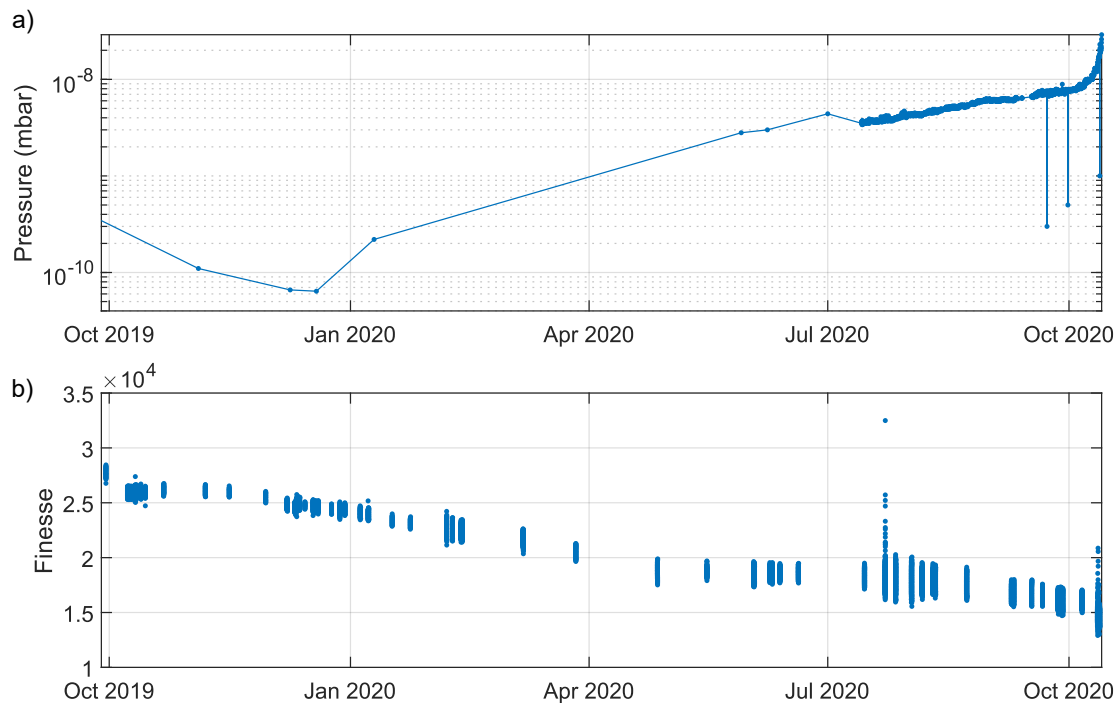


Figure B.1: In a), the pressure inside of the vacuum chamber over the course of this work is shown. In b), the decay of the finesse of the fiber cavity is shown.

Acknowledgements

First of all, I would like to thank Prof. Dieter Meschede for giving me the opportunity to work in his research group. I am very grateful for working on quantum technologies in such a motivated atmosphere and the insight into scientific research that was given to me. Furthermore, I thank him for his support and advise, particularly in regard with the present coronavirus. I thank Prof. Dr. Simon Stellmer for being my second advisor.

I would like to thank Dr. Wolfgang Alt for lively discussions about all kinds of physical phenomena. He was always open to discuss the daily lab problems and helped solving them with his experience. I am also very grateful for the always available Dr. Tobias Macha, Dr. Deepak Pandey and Dr. Hannes Pfeifer for sharing their experience in many different matters.

The work presented in this thesis would have not been possible without the FCQED team. Especially, I would like to thank Eduardo Uruñuela. He has been a constant source of stimulation and encouragement to me. His much appreciated guidance shaped this thesis and was very valuable in scientific and not so scientific topics. Special thanks goes to my office mates, Maximilian Ammenwerth, Pooja Malik and Madhavakkannan Saravanan. The time we spent in and out of the office was really nice and I am grateful for all the shared experiences. Let's always remember that time is not our aim.

I also want to thank all other present and past group members for the enjoyable time at the institute. In addition, I thank my fellow group members and Paul Meder for proofreading my thesis and/or listening to my colloquium trials.

Finally, I would like to thank my parents, my sister Neele and all my friends. They helped me with great support and distraction whenever I needed it.